Università degli Studi di Cagliari

DOTTORATO DI RICERCA

Scienze e Tecnologie per l'Innovazione

Ciclo XXXII

TITOLO TESI

Grain boundary segregation as the process enabling thermodynamic stability in nanocrystalline metal alloys

Settore scientifico disciplinari di afferenza

ING-IND/22

Presentata da:	Francesco Torre
Coordinatore Dottorato	Prof. Roberto Orrù
Tutor	Prof. Francesco Delogu

Esame finale anno accademico 2018 – 2019
Tesi discussa nella sessione d'esame Gennaio-Febbraio 2020

And following our will and wind
we may just go where no one's been
we'll ride the spiral to the end
and may just go where no one's been.

(Maynard James Keenan, Tool)

Table of contents

1. Introduction

The appearance of man at the dawn of times, the development of civilization, the rise and fall of Empires, the conquests of human intelligence have been allowed and intrinsically shaped by materials. From prehistory to present times, any real advance of man in its long journey from created to creator has been inextricably intertwined with the use of elements and substances or simple combinations of these, first, and, then, the design and fabrication of new materials.

The indissoluble link between man and materials is properly summarized by the motto "Materials by themselves do nothing; yet, without materials man can do nothing"[1]. It is even believed that cultural traits such as the use and the fabrication of tools deeply affected human brain and manual capabilities[2,3]. Therefore, it is no surprise that stone, copper, bronze, iron marked the main achievements of mankind across its ages. Mastering metallurgy, in particular, was key to a technological progress that projected man into social and economic realities of increasing complexity, eventually leading to irreversible changes in the paradigms governing human life and thought[4].

Revolutions took millennia and centuries to take place. Surprisingly enough, less than 12 materials had widespread use until 100 years ago. However, in the last decades wood, clays, iron, copper, gold, silver and a few plastics have been complemented at an ever-increasing rate by a variety of materials[5]. Some of these do better, or cheaper, what older ones did. Others combine properties allowing entirely new devices to be made or quite new effects to be obtained.

Pushed really by the need of identifying new materials and innovative solutions for product design going beyond simple combinations, a new science was born in the 1950s. At the intersection of physics, chemistry and engineering, materials science emerged as a new multidisciplinary field of study with microstructure as the best distinctive subject[6]. Quite soon, it firmly established itself as the science focusing on the relationship between structure and microstructure, on the one hand, and physical and chemical properties, on the other.

The scientific breakthroughs obtained have triggered dramatic changes in engineering and technology, thus giving rise to a virtuous feedback mechanism between basic and applied

knowledge that nourishes and shapes modern societies[1,7]. Semiconductors represent a glaring example[8], with their capability of paving the way to the advent of electronics and, then, of a completely new era for man. Another example is the spontaneous hardening of aluminium alloys due to the slow precipitation of copper at room temperature, which has revolutionized the aeronautic industry and suggested new strategies for fabricating new families of metal alloys[1]. Examples involving ceramics, polymers and composites can be added up.

With the aim of obtaining specifically tailored properties, a number of new materials have been identified and investigated. The profound evolution of materials science can be readily summarized in simple plots emphasizing the phenomenological relationship between different properties[9]. Although research in the field has unavoidably lived an empirical approach, the increasing computational power has soon led to a more efficient theory- and computationally-driven attitude[7]. Accordingly, multiscale modelling has begun to show its promise in terms of property prediction and material design[7,10].

Within this context, nanocrystalline (NC) metals represent a paradigmatic case. They form one of the most intensely investigated classes of materials[11–15]. Characterized by a polycrystalline structure with mean grain size on the nanometer range, NC metals exhibit unique physical and chemical properties with no parallel in their bulk counterparts. For instance, NC metals and metal alloys exhibit higher hardness, yield strength, elastic limit and thermal shock resistance as well as excellent wear resistance, lower friction, increased catalytic activity, superior soft magnetism and high electrical resistivity[16,17]. This makes NC metals and metal alloys attractive for a broad range of applications spanning the most diverse areas of science and engineering[18].

In general, NC metals and metal alloys seem to be particularly suited for applications requiring the combination of enhanced mechanical and functional properties[16,19]. However, reduced grain size and the consequent high volume fraction of grain boundaries (GBs) also result in the increase of Gibbs free energy, which renders NC metals prone to coarsening and the nanostructure intrinsically unstable. Such structural instability is particularly evident in non-refractory NC metals, which undergo grain growth at very low homologous temperatures or even at room temperatures. As a consequence, coarsening processes eventually depress the properties associated with the NC status of the material[20–23]. In contrast, NC alloys have

been shown to possess higher stability than their single-component counterparts[24–32]. While this behaviour has been traditionally ascribed to kinetic factors[33], the idea that some NC alloys can benefit from a thermodynamic stabilization related to solute enrichment at GBs was firstly proposed by Weissmüller[34], and is now widely accepted. In fact, while kinetic stabilization can only delay the grain growth process at low homologous temperatures, the thermodynamic approach has shown to be effective even at high temperatures for long time[28,32].

In the light of the great promise shown by metal alloys in terms of possible application, research on coarsening-resistant NC alloys has been increasingly supported by U.S. governmental actions - e.g. the Materials Genome Initiative[35] - and agencies - e.g. the National Science Foundation[36]. Meanwhile, also the European Commission supported this topic within the Future and Emerging Technologies programme of H2020 platform, funding the ICARUS (Innovative Coarsening-resistant Alloys with enhanced Radiation tolerance and Ultra-fine–grained Structure for aerospace application) project[37].

It is within the ICARUS project that the present thesis has been born and developed. It focuses on two main issues. First, the development of a general thermodynamic model that could give indication about the stability of multicomponent NC metal alloys against coarsening and precipitation of second phases. Second, the fabrication and characterization of NC metal alloys aimed at validating the statistical thermodynamic modelling by comparing modelling predictions with specific experimental case studies.

2. Nanocrystalline metals and metal alloys

It is well known that solid metals and metal alloys have a polycrystalline structure. Accordingly, the solid consists of grains of irregular shape that tessellate the space, thus forming a three-dimensional mosaic, as can be seen in the 3D simulation reported in Fig. 2.1a. Neighbouring grains are separated by GBs, i.e. interfaces that interrupt the periodicity of crystalline planes within each grain (Fig. 2.1b). Such interruption GBs stem from the misorientation of the crystalline lattice in adjacent grains and, therefore, exhibit a certain degree of structural disorder. Specifically, atoms located at grain boundaries are no longer able to occupy regular lattice sites in one or the other adjacent grains and appear to have intermediate position between the two. Such inefficiency in the packing of the atoms results in the generation of free volume at GBs. This can be observed in the transmission electron microscopy (TEM) micrograph reported in Fig. 2.1c, where dark dots are periodically observed along the interphase of two neighbour grains, highlighting the interruption of the lattice order.

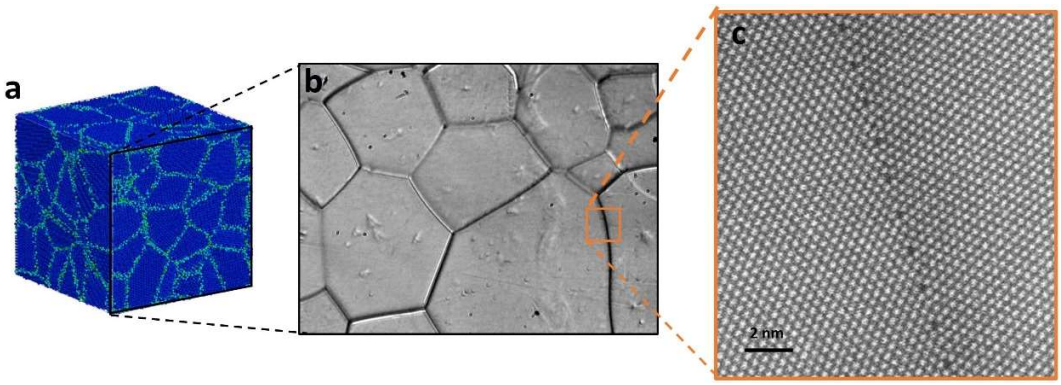

Fig. 2.1. (a) 3D simulation of a polycrystalline metal; **(b)** metallographic microscope image of a ruthenium sample[38]; **(c)** high resolution TEM micrograph of a GB in polycrystalline gold[39].

The displacement from equilibrium lattice position involves a local increase of potential energy and the result is a corresponding increase in the overall Gibbs, or Helmholtz, free energy of the solid.

As far as grains are on a coarse scale, the fraction of atoms involved in grain boundaries is quite small and, in general, negligible. It follows that their contribution to the Gibbs free energy of the solid is also negligible and the metal, or metal alloy, exhibits the well know spectrum of physical and chemical properties commonly associated with metallic solids. However, as the grain size is reduced down to the nanometer range, the situation drastically changes. The fraction of atoms located at grain boundaries increases hyperbolically as the grain size decreases and it becomes comparable with the fraction of atoms located in the bulk of crystalline grains. Typically, this occurs for grains with characteristic lengths around 80 nm or shorter.

Under such circumstances, atoms located at grain boundaries give a significant contribution to the Gibbs free energy, also affecting physical and chemical properties as a consequence of the associated structural disorder and the resulting excess free volume. It is exactly the combination of structural disorder and higher potential energy that makes polycrystalline metals and metal alloys unique in terms of physical and chemical properties, so much to deserve the specific name of NC metals.

Actually, NC metals can be quite different from their bulk counterparts under several points of view. For instance, the increase of GBs heavily hinders the dislocation movement leading to an increase of hardness and strength values up to 4/5 times when grain size reaches the nanoscale. Electrical and magnetic properties are also heavily affected. A decrease of the electrical resistivity up to the 50% when exposed to magnetic field, known as giant magneton resistance, has been reported for different systems, making them appealing for magnetic recording devices; micro-electrical-mechanical (MEMS) devices, sensor, and high-performance magnets are other potential application[12,18]. Recently, it was also shown that NC metals could be used in shielding shells for fusion reactors for the production of energy from fusion reactions. Indeed, the high density of GBs and defects act as sink for He bubbles enhancing the radiation tolerance and in general reducing damages[40].

These are only some of the reasons that made NC metals one of the most intensely investigated subjects in the history of materials science, showing the promise of changing the paradigm of man's capability of shaping nature and giving rise to a rush for the new gold treasured by nanoscience and nanotechnology.

Even though NC materials can be easily achieved, nanostructure stability is of primary concern during subsequent processing and service operation. Therefore, the technological application of NC materials depends crucially on the improvement of their stability through the development of effective methods to suppress or retard grain growth. In this regard, understanding the scientific nature of instability and grain growth in NC microstructures is a criterion for allowing strategies for minimizing grain growth to be developed.

2.1. Thermal instability, or the big deal

NC metals and metal alloys tend to be unstable against grain coarsening due to the large volume fraction of GBs, which have an associated energetic penalty with respect to the bulk, GB-free, reference state. Such tendency to coarsening is particular evident in pure non refractory NC metals, which can undergo abrupt grain growth even at room temperature[23,41,42].

Typically, grain growth occurs via GB migration, i.e. the diffusion of single atoms from one grain across the boundary to the other grain. The mechanism can be described in terms of simplified reaction rate theory[43]. As coarsening proceeds, the atoms near GBs move from their initial lattice sites on one side of the GB to a final one on the opposite side of the GB. In principle, atomic displacements can occur in both directions, but they can exhibit different jumping frequencies, f, thus resulting in a net flux of atoms. Within the framework of reaction rate theory, frequency and direction of atomic displacements from one grain to the adjacent one are determined by the activation energies, $Q_{1\to2}^{GB}$ and $Q_{2\to1}^{GB}$, for the direct and inverse exchange processes. As schematically shown in Fig. 2.2, the atomic displacement from grain 1 to grain 2 involves the surmounting of an energy barrier $Q_{1\to2}^{GB}$ that is lower than the energy barrier $Q_{2\to1}^{GB}$ that must be surmounted by atoms leaving grain 2 and reaching grain 1. The difference in the two activation energies determines the difference in Gibbs free energy, dG, between the two structural states and makes atoms progressively rearrange into bigger grains, thus reducing the volume fraction of GBs.

The resulting GB migration rate, v, can be expressed as

$$v = M\frac{dG}{\lambda^3} = M\Delta P, \tag{2.1}$$

where M, λ and ΔP are the GB mobility, the interatomic spacing in GBs and the driving force for GB migration, respectively[43,44]. The GB mobility, M, exhibits an Arrhenius-like dependence on temperature, T,

$$M = \frac{\lambda^4}{h}\exp^{-\frac{Q^{GB}}{kT}}, \tag{2.2}$$

where h is the Planck's constant. Accordingly, higher temperature favours GB migration, and, then, grain growth.

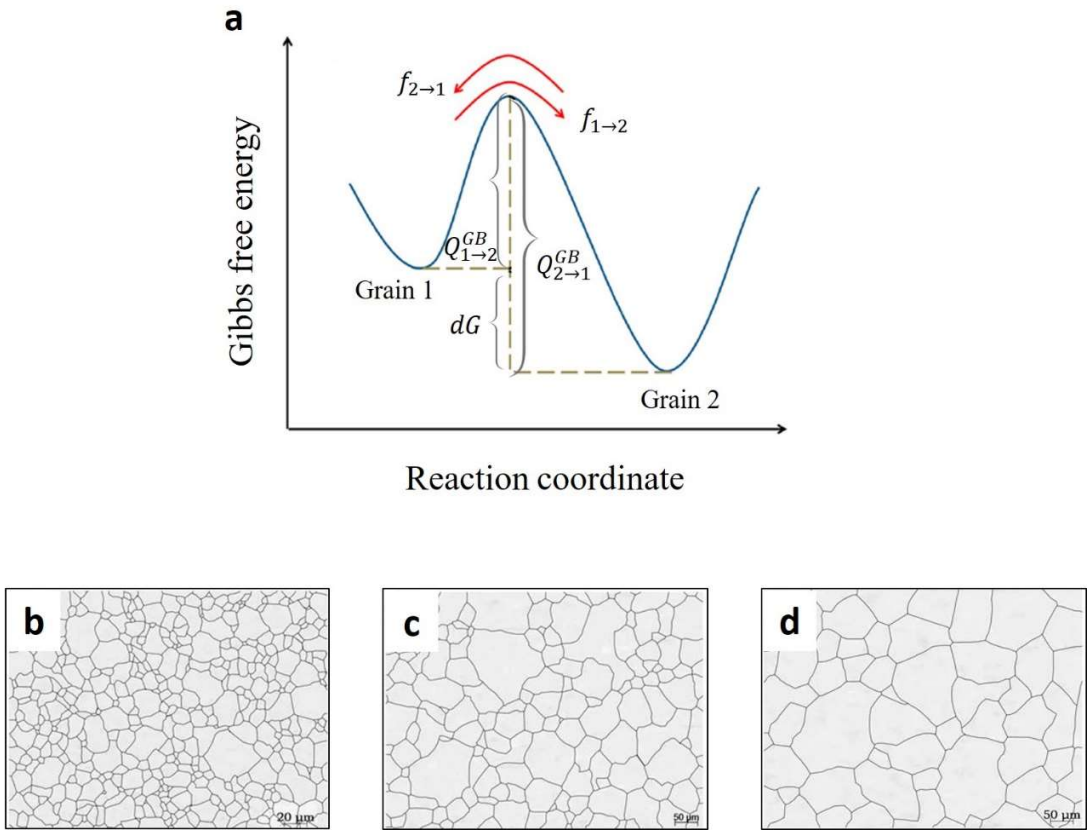

Fig. 2.2. Schematic representation of grain growth. **(a)** Gibbs free energy of lattice sites on opposite sides of a GB. $f_{1\to2}$ and $f_{2\to1}$represent the jumping frequencies of an atom from one side to the other side and *vice versa*[44]. The progressive decrease of GB surface during coarsening of a polycrystalline steel at **(b)** 850 °C, **(c)** 950 °C, and **(d)** 1100 °C[45].

The change in the Gibbs free energy, dG, provides the thermodynamic driving force to grain growth. For an elemental NC metal, dG corresponds to the reduction in Gibbs free energy resulting from the reduction of the GB area, dA_{GB}. Accordingly,

$$dG = \gamma dA_{GB}, \tag{2.3}$$

where γ is the excess energy per unit GB area. For elemental metals, GB energy is positive. It follows that a reduction of the GB area, i.e. an increase in grain size, determines a reduction of the overall Gibbs free energy.

This process makes NC metals and metal alloys intrinsically unstable and determines the coarsening of their structure. In turn, this involves the loss of most of the interesting physical and chemical properties imparted into the metal by the nanostructure. For this reason, grain growth must be hindered or, better, suppressed to enable any real practical application of NC metals in engineering. For instance, a potential use of NC alloys for turbines, whose efficiency increases with the increase of temperature, requires materials with high thermal capability[46]. Same for fusion plasma reactors; the increase of the radiation tolerance related to high GBs fraction, would be useful only if the NC microstructure can be retained at the operating temperature of the reactor itself.

Therefore, it is not surprising that the stabilization of nanostructures is hailed as one of the Holy Grails of Materials Science and Physical Metallurgy, i.e. one of those fundamental achievements capable of changing the face of human struggle taking steps along the long way towards the pursuit of knowledge and happiness.

2.2. Improving the stability of the nanostructure

Two deeply different, though partially overlapping, strategies can be evoked to hinder, and possibly suppress, grain growth[44,47]. On the one hand, kinetic strategies take inspiration from the capability of solute heteroatoms of pinning GBs via solute drag mechanisms. On the other, thermodynamic strategies aim at reducing the driving force to coarsening through a suitable reduction of the GB energy. In both cases, alloying is the key enabling factor and distinguishing its kinetic and thermodynamic effects is definitely challenging[48].

Kinetic stabilization relies upon the slowing down of GB migration through the increment of its activation energy. In turn, this can be induced by second phase drag[49], solute drag[50] and chemical ordering[51] processes that determine local rearrangements at GBs able to limit coarsening, especially for short annealing at moderate temperatures[52]. However, the nanostructure maintains its metastability with respect to the coarse-grained polycrystalline state, which leaves the driving force for grain growth unaltered. Thus, even a drastic reduction of GB mobility due to alloying-related processes can be eventually overcome at high temperature, enabling grain growth accordingly[53,54].

Thermodynamic stabilization aims exactly at tackling any issue related to the metastability of the nanostructure by making it the most, or nearly the most, stable state[34]. This would definitely suppress grain growth removing the underlying thermodynamic driving force. In analogy to the case of microemulsions[55], such result can be, in principle, obtained by the segregation of solute elements at GBs, which can cause a significant reduction of the GB energy up to vanishingly small, or even negative, values. Correspondingly, thermodynamic stabilization can be effective also at high temperatures[32], since the GB energy reduction through segregation exhibits only weak temperature dependence[53]. Under such circumstances, NC metal alloys can retain their structure for longer time at higher temperatures.

2.3. Solute segregation at grain boundaries

Inhibition of grain growth in NC metals via the reduction of GB energy was first addressed by J. Weissmüller in 1993[34]. The idea is based on the reduction of GB energy as a result of the inhomogeneous distribution of alloy components due to the tendency of some of them of occupying preferentially GB sites. Specifically, lower GB energies result from segregated atoms forming more favourable chemical bonds and reducing elastic mismatch strains because of the excess free volume localized at GBs[56]. The difference between sites within grains and at GBs allows uneven partition of the metallic species and a lower overall potential energy. Such inhomogeneous distribution is clearly pointed out by the chemical mapping of Au in a Pt-10 at.% Au alloy annealed at 775 K reported in Fig. 2.3 [57].

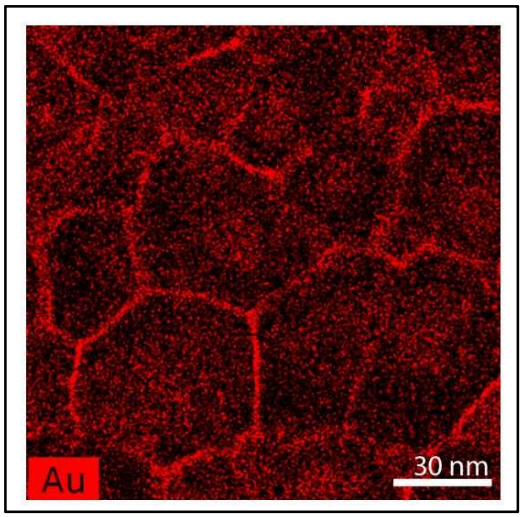

Fig. 2.3. Chemical mapping of a Pt-10 at.% Au alloy annealed at 775 K [57]. The distribution of elemental species highlights the clear tendency of Au to segregate at GBs.

Using the Gibbs adsorption equation in the dilute limit[58] to describe GB segregation in polycrystalline structures under the assumption of a McLean-type scenario[59], J. Weissmüller showed that dilute binary metal alloys can have significantly lower GB energies, γ, than those, γ_0, of the elemental metal. In particular, the GB energy of the alloy can be expressed as

$$\gamma = \gamma_0 - \Gamma\,(\Delta H^{seg} + kTlnX), \tag{2.4}$$

where Γ is the solute excess at GBs and ΔH^{seg} is the GB segregation energy, which corresponds to the energy difference that a solute atom experiences when it moves from a GB site to a lattice site within the interior of crystalline grains.

Following J. Weissmüller's contribution, several attempts have been made to gain insight into the mechanism of GB energy reduction and the role of solute distribution in binary metal alloys[60–64]. In general, the proposed models are based on quite severe assumptions that restrict the case studies to dilute solid solutions with high segregation tendency. Similarly, various models neglect chemical contributions to segregation[65–68], or assume only ideal bonding interactions[69,70]. In spite of this, NC metal alloys investigated experimentally are typically non-dilute alloys and solutes do not necessarily exhibit strong tendency to segregation[44,47].

An improved description of the stabilizing effects of GB segregation has been given by models based on statistical thermodynamics[44,71–77], recently reviewed and compared[78,79]. In particular, the statistical approach developed by J. Trelewicz and C. A. Schuh allowed extending the thermodynamic analysis to a metallic nanostructure including three structural components[71]. Their so-called regular NC solution (RNS) model provided a first general tool able to describe the Gibbs free energy of mixing in binary alloys including both crystalline grain and GB atomic environments. The RNS model reduces properly to a regular solution model[80] for a crystalline phase in the limit of infinite grain size and to a standard GB segregation isotherm in the dilute limit. Specifically, the model introduces an intergranular phase, i.e. a GB phase, that separates grains from each other and an interface that marks the transition from grain interior to intergranular region. Accordingly, the NC structure can be regarded as a network of atoms and chemical bonds arranged to form grains with average diameter d and intergranular layer thickness t. The schematic description of such NC structure is given in Fig. 2.4.

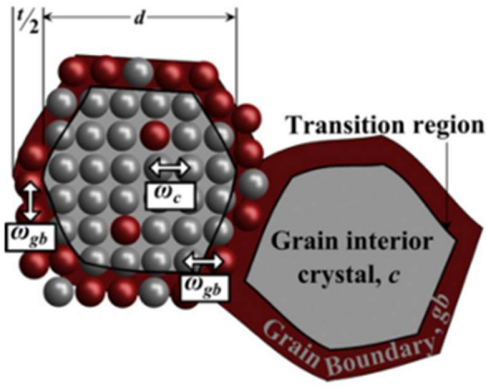

Fig. 2.4. Schematic depiction of two NC grains exhibiting grain boundary segregation, represented equivalently as an array of atoms (left) or as a continuum (right). Grey and red indicate, respectively, solvent and solute atoms. The characteristic grain size, d, and GB thickness, t , are shown. Arrows denote the interactions considered within the RNS model[71,73].

Two interaction parameters are used to account for the energy differences experienced by atoms located in GBs and in grain interior, namely ω_{gb}, and ω_c, which represent the chemical bond energy in the crystalline bulk and in GB and transition regions respectively. The

enthalpy of mixing, i.e. the change in enthalpy associated to the formation of the NC solid solution and calculated respect to the pure elements in their reference state, results from the sum of the energy, ω, associated with all the possible atomic pairs in each of the three bonding regions[71]. Following the standard statistical approach[80], the entropy of mixing equals the one of a random distribution of atoms over distinct atomic sites. Thus, the Gibbs free energy of mixing of a general polycrystalline binary metal alloy can be expressed as

$$\Delta G_{mix} = (1 - f_{ig})\Delta G^{b}_{mix} + f_{ig}\Delta G^{ig}_{mix} + zvf_{ig}\left\{\left[X_{ig}(X_{ig} - X_b) - (1 - X_{ig})(X_{ig} - X_b)\right]\omega_{ig} - \frac{\Omega}{zt}(X_{ig} - X_b)(\gamma_B - \gamma_A)\right\}, \quad (2.5)$$

where ΔG^{b}_{mix} and ΔG^{ig}_{mix} are the Gibbs free energy of mixing in the bulk and in GBs, and f_{ig}, z, v, Ω, γ_A and γ_B are the volume fraction of GBs, the coordination number, the transitional bond fraction, i.e. the fraction of atoms at the interface between the bulk and the GB regions, the atomic volume and the GB energy of component A (matrix) and component B (solute) respectively.

Then, the equilibrium condition for the nanostructure can be identified by minimizing Eq. 2.5 with respect to the chemical composition of the intergranular region and its volume fraction. In particular, the intergranular volume fraction was indirectly traced back to the grain size by making geometric assumptions on the grain shape[71]. This allows relating the equilibrium grain size, d, to the amount of solute, X. Interestingly, the $d - X$ trend predicted by the model agrees with experimental evidence regarding binary alloys showing a strong thermodynamic contribution to their stability[25,53,63].

Subsequently, C. A. Schuh and co-workers[32] and Darling *et al.*[65] showed that the RNS model could be used to design thermodynamically stable metal alloys. To this aim, the former introduced stability maps relating enthalpy of mixing and enthalpy of segregation, i.e. the difference in energy of a solute atom occupying a grain boundary site vs a grain interior site, such as the one shown in Fig. 2.5a. Similarly, the latter proposed the elastic enthalpy, i.e. the contribution due to the elastic misfit, and enthalpy of mixing, as shown in Fig. 2.5b. The solute elements able to stabilize the matrix element, e.g. W or Fe, can be identified by their position in the map.

For instance, let us consider the stability map in Fig. 2.5a. It concerns W-based alloys. The Gibbs free energies of NC structure, two-phase state corresponding to phase separation and coarse-grained solid solution are compared for the solutes Sc and Ag. In the former case, the nanostructure has a Gibbs free energy lower than those of both coarse-grained and phase-separated phases. Correspondingly, the point representing the W-Sc alloy lies in the portion of the map indicating stability for the nanostructure. In contrast, for the W-Ag alloy the Gibbs free energy of the coarse-grained regular solution is lower than that of the nanostructure. Accordingly, the point representing this alloy lies in the portion of the map indicating that bulk is the most stable phase. In agreement with the stability map indications, a NC W-20 at.% Ti alloy exhibits a superior thermal stability against grain coarsening, undergoing negligible grain growth after annealing at 1373 K for one week[32]. Microscopic evidence showing Ti segregation at GBs supports the hypothesis of thermodynamic stability[48]. Other binary alloys that were selected based on the RNS model such as Fe-Mg[81], W-Cr[82] and Fe-Au[83] showed significant thermal stability enabled by GB segregation.

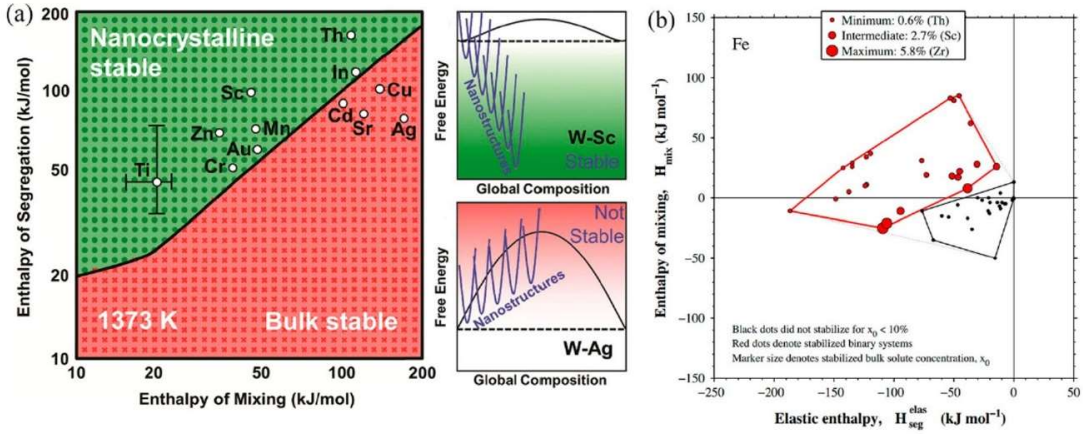

Fig. 2.5. (a) Stability map for NC W-based binary alloys containing different solutes at 1373 K. Green and red regions correspond, respectively, to stability and instability regions for NC alloys[32]. **(b)** Stability map of NC Fe-based binary alloys for stabilizing (red dots) and non-stabilizing (black dots) solutes. The size of red dots accounts for the solute concentration needed to stabilize a grain of 25 nm[65].

Due to the excellent results obtained in designing coarsening-resistant binary NC metal alloys, other researchers attempted similar approaches involving the removal of the transition interface or the effects of GB excess volume[72]. Additional elastic contributions to the total Gibbs free energy have been also taken into account[76], which allows dealing with alloys with heat of GB segregation affected by elastic contributions[77].

It is also worth noting that most of literature remain focused on binary metal alloys, with only a few case studies concerning ternary ones[68,75,84–87], despite the considerable scientific and technological interest in multinary metal alloys. Multicomponent NC metal alloys are also expected to display atomic configurations not accessible to binary alloys[84], which can impart them, at least in principle, a broader spectrum of physical and chemical properties and makes thermodynamic stability more probable. Indeed, a larger number of alloy constituents results in an impressive increase of possible element combinations and, thus, of alloy compositions that can exhibit thermodynamic stability. For this reason, only a model-driven alloy design can mitigate the efforts related to a systematic experimental investigation, allowing a preliminary screening of potentially interesting NC metal alloys. In this regard, computational screening efforts have been already undertaken and new interesting alloy compositions are continuously added to web-based repositories.

2.4. Aims and objectives

The present work aims exactly at developing a formal thermodynamic framework enabling the description of NC metal alloys involving an arbitrary number of elemental constituents and phases. To this aim, we consider the thermodynamic effects of an inhomogeneous partition of solutes within a NC microstructure consisting of crystalline grains embedded in a continuous, percolating GB network.

Enabling the evaluation of GB contributions to the alloy thermodynamics, the model can be used to accomplish three fundamental objectives. First, a general systematic screening of binary metal alloys to gain information on the impact of GB segregation on the relative thermodynamic stability of alloys characterized by quite different chemical composition in terms of elemental species and nominal stoichiometry. Second, the identification of candidate

alloys capable of attaining the highest possible resistance to coarsening under thermal annealing conditions. Third, the design of specific metal alloys characterized by enhanced thermal stability in connection with their possible application.

In this respect, the present thesis also aims at the experimental validation of the thermodynamic model. Accordingly, two additional objectives emerge. On the one hand, the experimental investigation of suitable case studies that can provide reasonable support to theoretical predictions. On the other, the fabrication of innovative metal alloys that can find application in areas of science and engineering interested in metals rich in interfaces. For these reasons, we focused on W-based alloys. Not only energetic parameters are available for a reasonable number of cases, but also W-based alloys can be utilized as structural materials in harsh environments affected by irradiation conditions. The experimental evidence, discussed in literature[32,82], that NC W-based alloys can actually exhibit thermodynamic stability represents a further advantage.

3. A generalized thermodynamic model

The thermodynamic modelling developed in the present work has taken inspiration from the statistical thermodynamic approach proposed by J. Trelewicz and C. A. Schuh in their seminal paper published in 2009[71]. Their so-called RNS model introduced an original point of view in the field, allowing a re-interpretation of the classical regular solution model applied to crystalline solutions and deeply innovating the possible design strategies to obtain thermodynamically stable NC metal alloys. Specifically, the RNS model developed by J. Trelewicz and C. A. Schuh[71] paved the way to the design of different NC metal alloys that can achieve thermodynamic stability against grain coarsening based on GB solute segregation.

Briefly, the RNS model extended the regular solution model to binary NC alloys by explicitly including energetic contributions of GBs. This allowed the design of NC alloys showing thermodynamic stability against both coarsening and phase separation[88].

In a few cases, model predictions have found support in experimental evidence. In this respect, it is particularly meaningful the case of the W_{80}-Ti_{20} alloy[32,89]. Indeed, this system showed almost no grain growth after annealing at 1100 °C for one week. Experimental evidences of Ti segregation at GBs further confirmed that a thermodynamic stabilization was achieved.

Nevertheless, the RNS model is limited to binary systems. As further explained in the following, it is also based on arbitrary assumptions on GB thickness and bond distributions across the different regions of grains. While these assumptions may have a negligible effect in binary systems, their extension to the case of multi-grained, multicomponent materials structure is not straightforward.

Aimed at providing a more general thermodynamic model able to tackle suitably the limitations mentioned above, we improved the theoretical approach extending it to the case of multicomponent, multiphase NC metal alloys. Simultaneously, we replaced most critical assumptions with a coherent conceptual framework. Consequently, our model can be reduced to the RNS model under suitable conditions, which makes the RNS model a special case of ours.

Similar to the RNS model, our model describes a multiphase polycrystalline alloy as a collection of grains of q diverse grained (g) phases separated by a common intergranular (ig) region. The resulting structure is schematically depicted in Fig. 3.1. The model does not involve any transition surface between grains and intergranular region, thus assigning the energy contribution of GBs to their entire volume.

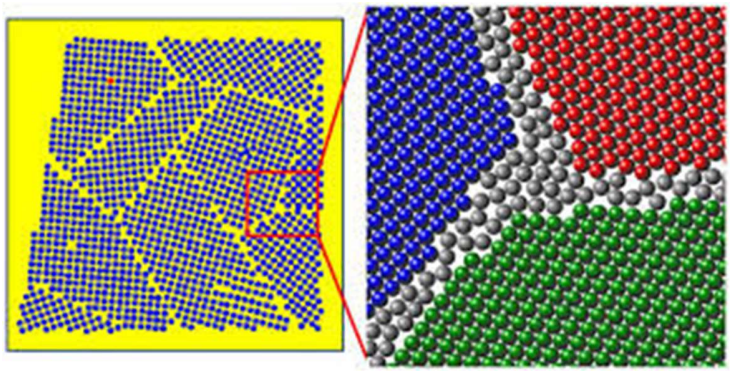

Fig. 3.1. Representation of multi crystalline solutions (colored areas) system with intergranular regions of a finite volume (white area).

Grained and intergranular phases consist of random solid solutions. We do not account for directional bonds, which involve the formation of ordered compounds. Indeed, the introduction of intermetallics in the adopted mathematical formalism is not straightforward, as it would imply the use of sublattices according with the quasichemical solution model[90]. Moreover, in the case of non-stoichiometric compounds, a non-homogeneous distribution of the different component, i.e. segregation, must also be considered. This would lead to a drastic increase in the model's complexity, i.e. a higher number of variables and parameters. Nevertheless, it will be shown that intermetallics can be subsequently included in the equilibrium phase diagrams in order to assess whether they are or not expected to affect the thermodynamic stability of the NC sold solutions.

An exhaustive derivation of the thermodynamic model is given in the Appendix to avoid weighing up the text. Here, we simply highlight the salient points.

The molar Gibbs free energy of mixing of the entire system includes the contributions of each grained phase as well as of the intergranular one. Every contribution is weighted based on the molar fraction of atoms, θ, belonging to the related phase

$$\Delta\hat{g}_{mix} = RT\left(\sum_{k=1}^{q}\theta^{(g_k)}\sum_{i=1}^{n}x_i^{(g_k)}lnx_i^{(g_k)} + \theta^{(ig)}\sum_{i=1}^{n}x_i^{(ig)}lnx_i^{(ig)}\right) + \sum_{k=1}^{q}\theta^{(g_k)}\Delta\hat{u}_{mix}^{(g_k)} + \theta^{(ig)}\Delta\hat{u}_{mix}^{(ig)} \quad (3.1)$$

Eq. 3.1 accounts for entropic contributions in terms of configurational entropy of random regular solution, where x_i^q is the molar fraction of component *i* in the *k* phase. More complicated are the terms describing the internal energy contributions of grained $\Delta\hat{u}_{mix}^{(g_k)}$, and intergranular, $\Delta\hat{u}_{mix}^{(ig)}$, phases. As for the regular solution model, any atom interacts with its nearest neighbours according to a pairwise chemical bond scheme. Within each phase made up of q components, atoms of a given component can have atoms of a different component among the nearest neighbours, which involves considering cross interactions. In each phase, any bond pair will exhibit a specific bond energy $u_{ij}^{(k)}$. In principle, bond energies $u_{ij}^{(k)}$ can differ from phase to phase. The nature of atoms involved being the same, $u_{ij}^{(k)}$ can also differ from grained to intergranular phases.

The molar fractions of the different phases can be related to their volume fractions according to the equation

$$f^{(l)} = \frac{\theta^{(l)}\sum_{i=1}^{n}\Omega_i x_i^{(l)}}{\sum_{k=1}^{q}\left(\theta^{(g_k)}\sum_{i=1}^{n}\Omega_i x_i^{(g_k)}\right)+\theta^{(ig)}\sum_{i=1}^{n}\Omega_i x_i^{(ig)}};\ l = g_k, ig; k = 1,..,q. \quad (3.2)$$

where Ω_i are the atomic volumes of the *i* component. In the presence of a geometric assumption, the volume fraction of the GBs can be related to the grain size. A possible choice[71] leads to the expression

$$f^{(ig)} = 1 - \left(\frac{d^{(g)}-t}{d^{(g)}}\right)^3 \quad (3.3)$$

between grain diameter, d, volumetric fraction, f, and GB thickness, t. In the literature[71], t was given the value of 0.5 nm. However, Eq. 3.3 and similar ones cannot be straightforwardly extended to the general case of multicomponent alloys characterized by the coexistence of

two or more grained phases. For this reason, it is preferable, at least in general, to assess thermodynamic stability in polycrystalline alloys with reference to volume fractions and not specifically to grain-related concepts.

3.1. Model parameters

Parameter values deeply affect the reliability of model predictions. While this is true in general for models, the issue is particularly evident in the case of models involving physical and chemical quantities related to GBs. In our case, model predictions can be expected to depend on GB energy, $\gamma_i^{(ig)}$, GB molar surface, $\hat{a}_i$, of components, interaction energy in the grained phase, $\omega^{(g)}$, and interaction energy in GBs, $\omega^{(ig)}$.

3.1.1. Enthalpies of mixing

It can be reasonably assumed that $\omega^{(g)}$ equals the interaction energy in the bulk, $\omega^{(b)}$, which, in turn, is related to the enthalpy of mixing for the solid solution. Empirical or semi-empirical approaches can be used to estimate the interaction parameters. The method developed by A. R. Miedema and co-workers is particularly suited to estimate mixing and formation enthalpies of solutions and compounds[91–93] and has been already applied to thousands of binary systems.

According to the Miedema's approach, the molar enthalpy of mixing of two generic elements can be expressed as

$$\Delta H_{mix} = \Delta H_{mix}^{(chem)} + \Delta H_{mix}^{(elast)} + \Delta H_{mix}^{(struct)} \tag{3.4}$$

where the first term considers the liquid-like interactions between atoms, the second accounts for the elastic mismatch due to the atomic size difference between elements and the third measures effects of chemical composition on the crystalline lattice selection for the alloy. Difficult to evaluate[93,94], the structural term is neglected in the vast majority of literature concerning the Miedema's model. Nevertheless, it has been shown to affect several systems, improving thermodynamic predictions[92,95].

Specifically, the so-called structural term can play an important role in those cases where the Miedema's model results in unphysical predictions, such as negative enthalpies of mixing in systems showing a significant miscibility gap. This is also the case of W-Ti. While it is highly immiscible[96], the Miedema's model predicts a negative enthalpy of mixing, which pushed C. A. Schuh and co-workers to use an experimental estimate of the enthalpy of mixing[32]. Unfortunately, experimental estimates are often lacking.

Enthalpies of mixing can be profitably estimated using CALPHAD-based methods to best fit experimental phase diagrams. For instance, the Redlich-Kister (RK) equation allows estimating the excess molar Gibbs free energy of mixing[97]. *Ab initio* calculations and atomistic simulations based on molecular dynamics and Monte Carlo methods can be utilized as well to estimate interaction energies in grained phases and GBs.

All the methods mentioned above exhibit limitations and raise difficulties. For instance, the RK method requires reliable experimental information that are not always available. *Ab initio* calculation and atomistic simulations are usually time consuming and may require a significant computing power.

3.1.2. GB-related parameters

GB energy of pure components depends on temperature, pressure and degrees of freedom of the GB[59,98]. Relatively accurate estimates have been obtained using first-principle[99]and molecular dynamics[100] calculations. Moreover, machine-learning approaches have recently been proposed as alternative methods[101]. However, it is customary to assume that, to a first approximation, GB energy is approximately equal to one third of the surface energy of the pure component in contact with vacuum[102]. An analogous approach holds for the molar surface[103], $\hat{a}_i$, and the molar surface energy of pure components at the GBs, $\hat{a}_i\gamma_i^{(ig)}$. An even rougher approximation was proposed by C. A. Schuh and co-workers, who assumed that the same average value of 8.25 *kJ/mol* can be used for all the alloys[32,73].

In contrast, we took advantage of the databases provided by H. Bakker[93] to evaluate the molar surface energies of pure components at GBs. Accordingly, we have values ranging between 1.5 and 15.5 *kJ/mol* as shown in Table 1. Not only this imparts the model with

broader generality, but also allows more accurately describing the energetic contribution of different elements to GB formation and GB solute segregation.

Unfortunately, the most important quantities affecting the stability of polycrystalline and, especially, NC alloys, i.e. the interaction parameters at GBs, $\omega^{(ig)}$, are also the most difficult to obtain. No reliable method to estimate their values is available in the literature. Thus, $\omega^{(ig)}$ is simply expressed as

$$\omega^{(ig)} = \beta\omega^{(b)} \tag{3.5}$$

where β is an adjustable parameter[104,105]. Sometimes its value has been taken constant[106], sometimes it has been estimated via the segregation enthalpy.

3.2. W-based binary alloys as benchmark to test the model

Binary alloys represent the simplest case to investigate. Not only a smaller number of independent variables and parameters is needed, but also experimental evidence mostly concerns binary alloys. In particular, thermodynamically stable nanostructures have been reported for W_{85}-Cr_{15}[82] and W_{80}-Ti_{20}[32,89]. It follows that W-based alloys represent the best case study to test model predictions and validate the modelling approach.

3.2.1. Theoretical assessment of thermodynamic stability

In order to analyze the thermodynamic stability of polycrystalline solid solutions, possible stable (equilibrium) states need to be identified. According to expression of the molar Gibbs free energy of mixing given by Eq. 3.1 there are four possible states in the case of a binary system; two mono-phasic and two bi-phasic. Mono-phasic states are represented by systems where the bulk phase (b) or the intergranular regions (ig) only is present. A classic phase separated state comprising two bulk phases (b_1 and b_2) is also possible. Finally, a state where the grained (g) and the intergranular regions coexist correspond to the latter one. The bulk phase ($\theta^{(g)} = 1$) corresponds to the single crystal condition and do not need any additional comment. Similarly, the two-bulk phase corresponds to a typical immiscible binary system. Instead, the other two possible states deserve further discussion.

System states where only the grain boundary region is present ($\theta^{(ig)} = 1$) were already hypothesized by Schuh and co-workers [71,74]. Although the physical counterpart of this theoretical outcome still need to be better identified, it should be pointed out that it logically derives from the mathematical formalism adopted. Moreover, the existence of the intergranular region is a necessary condition to define the state of the system characterized by the coexistence of the grained and GB phases. This state can be identified by the condition $0 < \theta^{(ig)} < 1$, which regardless of the specific relationship between molar and volumetric fractions and grain size, entails that the GB phase is present and that grain size has finite value.

The last thermodynamic state described above clearly identifies the polycrystalline system. It is then clear that according to the formalism adopted in this thesis, polycrystalline structures are not single-phase systems but rather the result of the co-existence of grained phase(s) and the intergranular (GB) region. It should be pointed out that the same conditions were used by Trelewicz and Schuh in their seminal paper to identify the nanostructured state[71]. However, as previously mentioned, a relationship between volumetric fraction and grain size should be provided to make a discrimination between coarse polycrystalline and NC structures based on grain size. For instance, a NC system is typically defined as a structure having grain size in the range between 0.5 and 100 *nm*. Assuming that $t = 0.5\ nm$, the $f^{(ig)}$ domain can be subdivided into the two intervals $0 < f^{(ig)} \leq 0.015$ and $0.015 < f^{(ig)} < 1$. Whereas the former interval represents the stability region of coarser structures, the second one identifies the stability range of nanostructures. However, this distinction will not be considered for the above-mentioned reasons, and the thermodynamic stability of polycrystalline systems will be investigated regardless the actual grain size. In this sense, the appearance of polycrystalline structure as the stable state could be considered a *conditio sine qua non* for the thermodynamic stability of nanostructures.

Once temperature and global composition are given, the equilibrium state of the system is identified by calculating and comparing the Gibbs free energy of mixing of all accessible states. The equilibrium state is the one characterized by the minimum of $\Delta\hat{g}_{mix}$. The Gibbs free energy of mixing of single-phase states can be easily evaluated, while multiphase states show a more complex picture. Let us consider as an example a dual-phase binary system at

constant pressure, temperature, and global composition. The following variables are needed to completely characterize the state of the system: $\theta^{(\alpha)}$, $\theta^{(\beta)}$, $x_A^{(\alpha)}$, $x_B^{(\alpha)}$, $x_A^{(\beta)}$, $x_B^{(\beta)}$, where α and β represent the two coexisting phases, regardless both of them are bulk phases or a polycrystalline state is involved. Taking advantage of material balances and congruency relations, it can be easily demonstrated that the independent variables describing a dual-phase binary system reduce to two. This means that the minimum value of $\Delta\hat{g}_{mix}$ for this state should be found by minimization in the two-dimensional domain defined by the two independent variables $x_B^{(ig)}$ and $\theta^{(ig)}$ (B indicating the solute in the W-based alloy). The pair $x_B^{(ig)}$- $\theta^{(ig)}$ giving the minimum of $\Delta\hat{g}_{mix}$ identifies the grain boundary composition and molar fraction, respectively, of the polycrystalline alloy to be compared with other possible thermodynamic states for stability prediction.

The present approach can be better understood by referring to Fig. 3.2. Here, the dimensionless molar Gibbs free energy of mixing, $\Delta\hat{g}^*_{mix}$, $(= \Delta\hat{g}_{mix}/\omega^{(b)})$ at 0 K of bulk solid solution (red), phase separated state (green) and intergranular phase (blue) are plotted as a function of the global composition. The latter one is depicted for different values of the coefficient β (Eq. 3.5), which is here taken as a free parameter in order to highlight how the interaction energy at GBs, $\omega^{(ig)}$, does affect the equilibrium state. In fact, different values of β correspond to different values of $\omega^{(ig)}$, according with Eq. 3.5.

As example, data related to the W-Zn are used in Fig. 3.2a. Indeed, this represents a typical strongly immiscible system. It can be seen therein that the molar Gibbs free energy of mixing of the grain boundary phase, $\Delta\hat{g}_{mix}^{(ig)}$, (blue) is higher that the bulk phase one, $\Delta\hat{g}_{mix}^{(b)}$, (red) whatever the alloy composition when $\beta = 1$. Under these conditions, polycrystalline structure is thermodynamically unstable compared to the bulk solid solution. Decreasing the value of β (down to 0 in Fig. 3.2a) a compositional range where the $\Delta\hat{g}_{mix}^{(ig)} < \Delta\hat{g}_{mix}^{(b)}$ appears. However, this is clearly a condition of metastability. Indeed, since $\omega^{(b)} > 0$ for the W-Zn alloy, the thermodynamically most stable state is represented by the phase separated system (green), whose molar Gibbs free energy of mixing, $\Delta\hat{g}_{mix}^{(\alpha\beta)}$, is zero at 0 K.

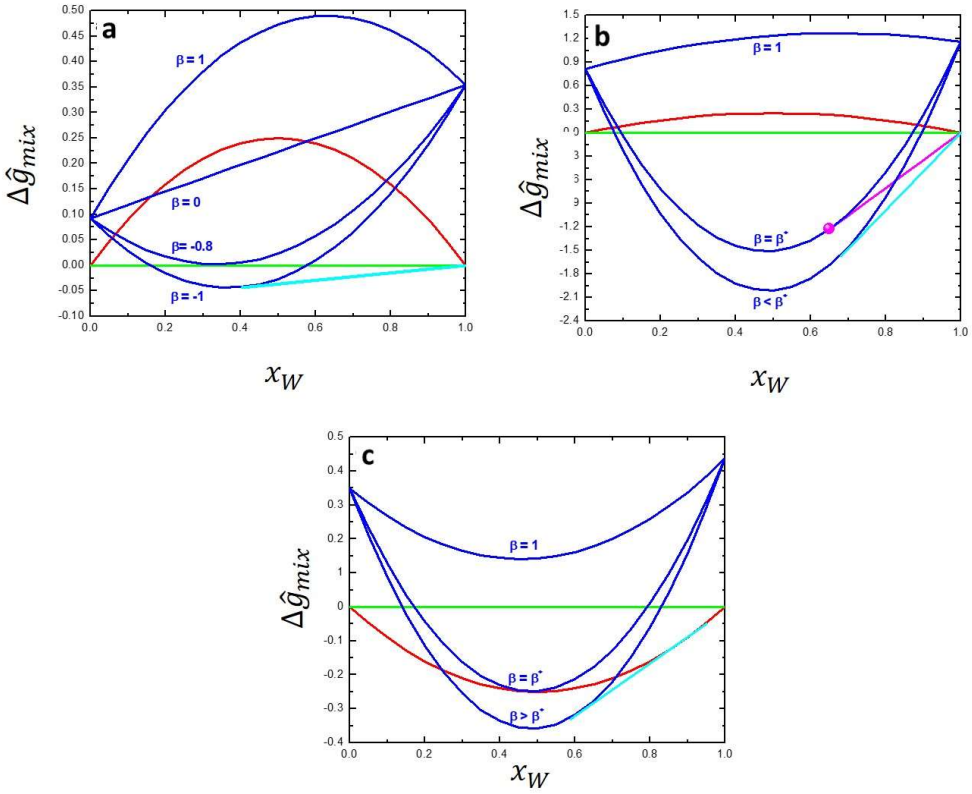

Fig. 3.2. Thermodynamic phase equilibria of polycrystalline alloys: a) W-Zn; b) W-Zr; c) W-Nb. Dimensionless Gibbs free energy as function of composition are reported for bulk solid solution (red), phase separated state (green), as well as grain boundary phase (blue). Latter one is depicted for different values of the coefficient β. Polycrystalline stable state are given the common tangent between grain boundary phase and bulk solid solution (cyan). Purple common tangent describes instead the existence of intermetallic-containing states.

By further decreasing the coefficient β, it will be reached a value ($\beta = -0.8$ in Fig.3.2a) such that there is at least one composition whose corresponding molar Gibbs free energy of mixing of the grain boundary phase is zero, i.e., $\Delta\hat{g}_{mix}^{(ig)} = \Delta\hat{g}_{mix}^{(\alpha\beta)}$. Let us identify this value as β^* and name it as the critical β coefficient. It can be then seen that a common tangent (cyan) between the pure tungsten phase and the grain boundary phase can be drawn when the condition $\beta < \beta^*$ is satisfied. Of course, the common tangent between the pure zinc phase and the grain boundary phase can be also drawn. However, it will be not here considered

since we are focusing on W-rich alloys. According to classical phase equilibria thermodynamics, such tangent represents bi-phasic stable states characterized by the coexistence of pure W grained (*g*) phase and intergranular (*ig*) one. It is then apparent that $\beta < \beta^*$ identifies a necessary condition for the polycrystalline structure to have thermodynamic stability in immiscible binary systems.

The same analysis illustrated in Fig. 3.2a can be extended to binary systems characterized by a positive value of $\omega^{(b)}$ and forming intermetallic compounds. Fig. 3.2b shows the case of W-Zr alloys at 0 *K*. Molar Gibbs free energy of the different phases are reported according to the procedure already illustrated in Fig. 3.2a. In addition, the point (magenta) characterizing the stoichiometric intermetallic compound W_2Zr is also shown. The molar Gibbs free energy of this compound, $\Delta\hat{g}_{form}^{(\gamma)}$, was taken equal to -11.63 *kJ/mol* as calculated by the Miedema's method[93]. The purple line represents the common tangent between the intermetallic phase and the pure tungsten one. Therefore, it can be seen that, for the case of $\beta = 1$, the stable states in the W-rich side are all a mixture of the just mentioned phases. This situation remains unaltered until the value of the coefficient β is decreased down to the critical value ($\beta = \beta^*$), which is equal to -9.99 per the case represented in Fig. 3.2b. Indeed, in such a situation, the molar Gibbs free energy of mixing of the grain boundary phase with the same composition of W_2Zr equals the molar Gibbs free energy of formation of this compound. Consequently, the critical parameter β^* can be defined as the value of the coefficient β such that $\Delta\hat{g}_{mix}^{(ig)}(x^\gamma) = \Delta\hat{g}_{form}^{(\gamma)}$, where x^γ represents the stoichiometric composition of the intermetallic phase γ.

A parallel investigation can be performed for those systems showing a negative interaction energy in the bulk, i.e., $\omega^{(b)} < 0$. As an example of these alloys, Fig. 3.2c illustrates the thermodynamic phase equilibria taking place in the W-Nb system. A critical value of the coefficient β can be identified also in this case. However, in this case β^* ascertains the condition $\Delta\hat{g}_{mix}^{(ig)} = \Delta\hat{g}_{mix}^{(b)}$ for at least one composition of this alloy. It can also be observed that the polycrystalline alloy is thermodynamically stable when the criteria ($\beta > \beta^*$) is fulfilled. Compositional range of these stable alloys is given in Fig. 3.2c by the common tangent (cyan), which represents the coexistence of the grain boundary phase (blue) and the grained solid solution (red).

The critical coefficient β^* has been calculated following the procedure illustrated in Fig.3.2 for all possible W-based metallic alloys. According with the three cases discussed above, the model results are grouped as follows: I) systems with $\omega^{(b)} > 0$ (Fig. 3.3a); II) systems with $\omega^{(b)} > 0$ forming intermetallic compounds (Fig. 3.3b); III systems with $\omega^{(b)} < 0$ (Fig.3.3c).

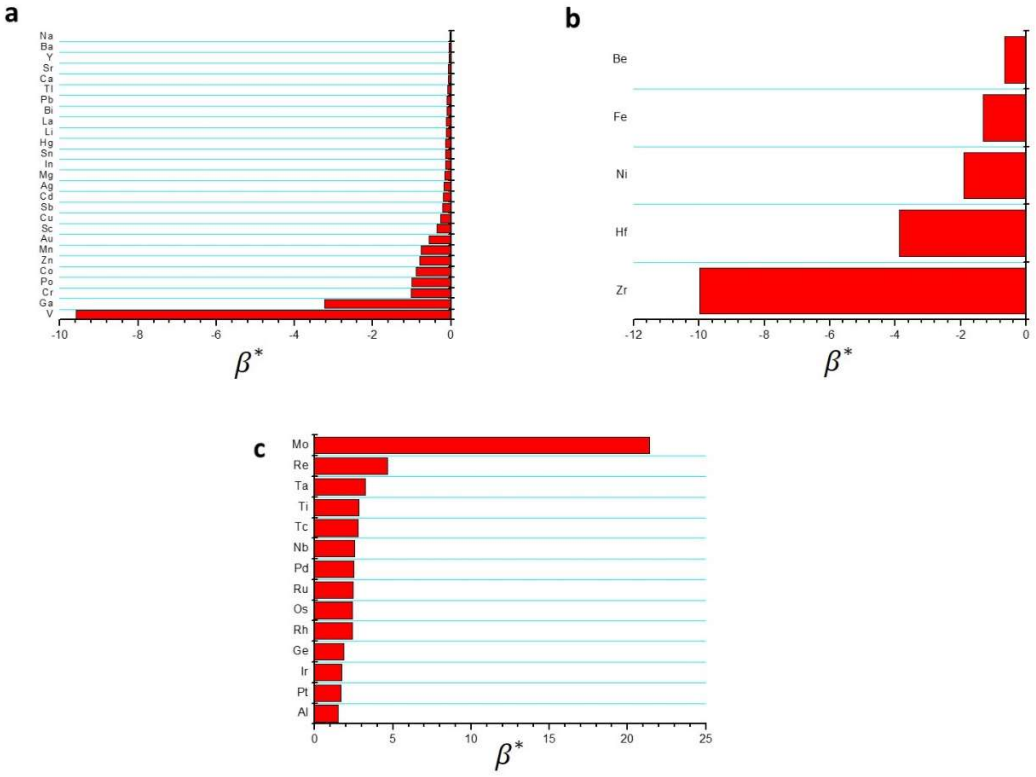

Fig. 3.3. Critical value of the coefficient β for alloys of group: a) I; b) II; c) III.

It is worth mentioning that a fourth group should be added, i.e., systems with $\omega^{(b)} < 0$ forming intermetallic compounds. However, among W alloys, only W-Al undoubtedly belongs to this group. Indeed, the existence of intermetallics at low temperatures in system W-X (X = Ge, Ir, Os, Re, Rh, Ru) is largely uncertain. Latter ones have been then analyzed according to group III rules, i.e., neglecting the formation of intermetallic phases. Regarding

the system W-Al, it will be investigated in details in the following, while, here a preliminary analysis of this alloy is given by neglecting the formation of WAl_4, i.e., group III.

A general overview of Fig. 3.3a shows that the critical coefficients β^* are all negative with no exceptions. The same finding can be observed in Fig. 3.3b, thus indicating that the effect of β in these alloys is dictated by the sign of $\omega^{(b)}$. The intermetallic formation certainly affects the magnitude of β^* but not its sign. Vice versa, a positive and greater that one value of β^* (again with no exceptions) is revealed for all system belonging to group III (Fig. 3.3c). It can easily demonstrated (Eq.3.5)) that the two stability criteria ($\beta < \beta^*$ for groups I and II, and $\beta > \beta^*$ for group III), can also be translated into the following one:

$$\omega^{(ig)} < \omega^* \tag{3.6}$$

where ω^* can be regarded as a critical value for thermodynamic stability occurrence. Latter parameter should satisfies the following conditions: $\omega^* < \omega^{(b)}$ and $\omega^* < 0$. It is important to highlight that both conditions do not depend on the sign of $\omega^{(b)}$ and that they should be simultaneously fulfilled.

The previous discussion highlighted how deeply the energetic parameters, and in particular $\omega^{(ig)}$, affect the model predictions about the equilibrium state. For this reason, parameters of W-based binary systems were carefully selected or estimated according with the procedure described in the following paragraph.

3.2.2. Selection of the parameters

We used the values calculated through the R-K method by G. Kaptay[107] to describe interaction energies between W and solute B in the grained phases, $\omega_{W-B}^{(b)}$. We also compared the values obtained through the R-K method and those estimated by the Miedema's approach with the aim of estimating the structural term in Eq. 3.4.

Apart from obtaining indications about the importance of the structural contribution to the enthalpy of mixing, this also allows an independent estimation of the interaction parameters at GBs. In this regard, it is worth noting that strain release and local disordering make the

elastic and structural terms drastically decrease at GBs. Therefore, it seems reasonable to neglect such contributions in the case of atoms located in the intergranular region. In contrast, the chemical contribution is completely unaffected. Then, the parameter β in Eq. 3.7 can be expressed as

$$\beta = \frac{\Delta\hat{h}_{B\to W}^{(chem)}}{\Delta\hat{h}_{B\to W}^{(chem)}+\Delta\hat{h}_{B\to W}^{(elast)}+\Delta\hat{h}_{B\to W}^{(struct)}} \tag{3.7}$$

The resulting β values are reported in Table 1 together with the other parameter values estimated for the binary W-based binary alloys.

Table. 1 Model parameters used for selected binary W alloys.

Solute	$\Delta\hat{\boldsymbol{h}}_{\boldsymbol{B\to W}}^{(\boldsymbol{chem})}$	$\Delta\hat{\boldsymbol{h}}_{\boldsymbol{B\to W}}^{(\boldsymbol{elast})}$	$\Delta\hat{\boldsymbol{h}}_{\boldsymbol{B\to W}}^{(\boldsymbol{struct})}$	$\boldsymbol{\beta}$	$\hat{a}_i\sigma_i^{(gb)}$
Ag	169.62	1.65	-10.77	1.05	5.53
Al	-53.47	0.55	38.93	3.82	5.05
Co	-5.07	49.65	-49.58	1.01	8.50
Cr	3.46	31.73	9.81	0.07	8.07
Cu	79.37	29.18	93.44	0.39	6.34
Mn	22.85	14.24	122.91	0.14	5.68
Mo	-0.87	0.14	2.23	-0.58	12.54
Nb	-33.39	7.09	-6.7	1.01	12.38
Ni	-11.32	52.92	-50.6	1.26	8.09
Re	-16.27	3.47	14.74	-8.38	14.45
Sc	38.34	48.57	-42.91	0.87	7.29
Ti	-22.41	3.60	51.81	-0.68	9.50
Y	110.41	90.61	-89.02	0.98	7.75
Zr	-38.59	46.10	-43.51	1.07	10.90

3.2.3. Comparison between model predictions and experimental results

Model predictions based on parameter values shown in Table 1 compare relatively well with experimental results reported in literature for some W-based alloys. Parameter values estimated using other literature methods give rise to definitely worse model performances[32]. A few examples regarding W-Ti[32] and W-Cr[82] are shown in Figs. 3.4a and 3.4b, respectively.

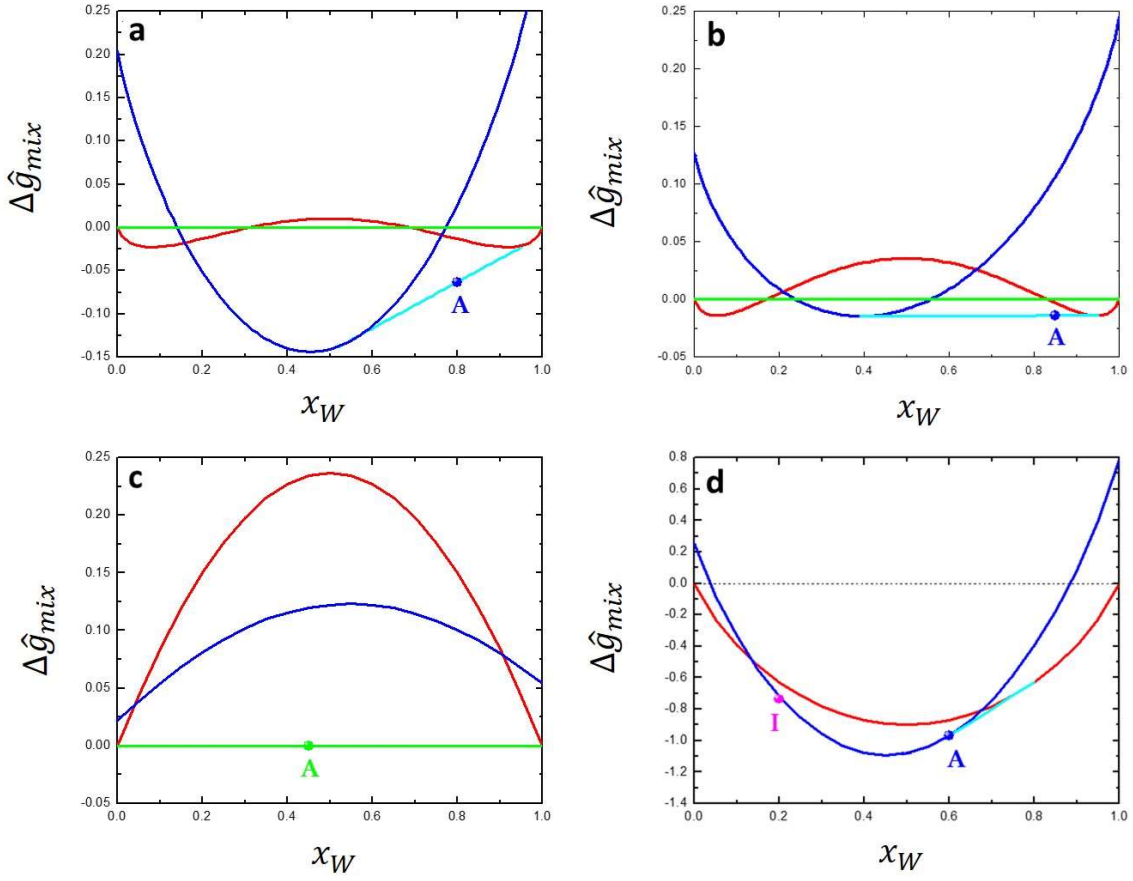

Fig. 3.4. Thermodynamic phase equilibria in the experimental investigated systems: **(a)** W-Ti; **(b)** W-Cr; **(c)** W-Ag; **(d)** W-Al. Dimensionless Gibbs free energy as function of composition are reported for coarse-grained solid solution (red), phase separated state (green), as well as grain boundary phase (blue). The common tangent (cyan) between grain boundary phase and bulk solid solution gives polycrystalline stable state. Points A are the predicted stable state of the experimental investigated alloys. The point I (magenta) in (d) refers to the stoichiometric intermetallic compound WAl_4.

It can be seen that, in Fig. 3.4a, the point representing $W_{80}Ti_{20}$ is located on the common tangent of the grained and GB phases. Therefore, the model correctly predicts that $W_{80}Ti_{20}$ is polycrystalline or NC. The polycrystalline structure exhibits the lower Gibbs free energy of mixing, thus indicating that the $W_{80}Ti_{20}$ alloy is thermodynamically stable at 1100 °C as experimentally observed[32]. Similar results were obtained for $W_{85}Cr_{15}$, which was found stable at 1400 °C[82] as shown in Fig. 3.4b.

Completely different is the W-Ag case. Curves in Fig. 3.4c show that the phase-separated state represents the most stable state for the whole compositional range at 800°C.

A few core statements can be made in the light of the thermodynamic behaviour of the three alloys considered. First, although thermodynamic stability is more likely for immiscible systems[88] due to the relationship between positive heat of mixing and GB segregation, immiscibility can also favour precipitation of the second phase. This seems to be the case of W-Ag.

Second, the stability of the polycrystalline structure improves when components have chemical affinity for each other at GBs. As a consequence, immiscible systems can reach thermodynamic stability at relatively low temperatures only if $\beta < 0$, i.e. if $\omega^{(ig)} < 0$. The W-Ti system can be regarded as a typical example in this sense. Its enthalpy of mixing is positive in the bulk and negative in GBs. This is in contrast with the W-Cr case, which has both $\omega^{(g)}$ and $\omega^{(ig)}$ positive. However, its positive mixing enthalpy in GBs is small enough to enable entropic stabilization at high temperature for the polycrystalline solid solution. Indeed, despite W and Cr are partially immiscible at low temperature, their alloy shows stability only for temperature high enough to bring the system within the miscibility region in the equilibrium phase diagram[82].

Third, the condition $\beta < 0$ is necessary but non-sufficient to stabilize polycrystalline structures. Indeed, the energy decrease emerging from the difference $\omega^{(ig)} - \omega^{(b)}$ has to balance the energy increase connected with GBs. Furthermore, it does not apply to systems characterized by a negative enthalpy of mixing in the bulk.

Taking into account the considerations mentioned above, we also selected candidate alloys among binary systems characterized by a negative enthalpy of mixing. In particular, our

attention focused on W-Al. As evident from Fig. 3.3d, the thermodynamic model predicts stability for a relatively broad compositional range at 1000°C. In addition, the presence of the ordered WAl_4 compound does not seem to affect the phase equilibrium of the W-rich W-Al alloys. For these reasons, we chose W-Al as a case study to investigate the capability of GB segregation of improving the stability of miscible NC alloys. Along the same line, W-Ag was chosen as a countercheck of model predictions, since they indicate a strong tendency to phase separation.

4. Methodologies

Thermodynamic modelling definitely shows that solute segregation at GBs can stabilize the structure of NC binary alloys to such an extent that the segregated nanostructure can become itself the most stable thermodynamic state. While this achievement marks the final moment of a long theoretical advancing towards a conclusive evidence, it represents a fundamental starting point to address experimental research in the fabrication of entirely new families of thermodynamically stable NC metal alloys. In this regard, challenges emerge in all their importance.

4.1. Fabrication of nanocrystalline metal alloys

Typically, the fabrication of nanostructured metals cannot rely upon conventional metallurgical methods[11,12]. To such aim, a broad spectrum of innovative methods taking advantage of far-from-equilibrium conditions have been developed ranging from vapour deposition to rapid solidification and severe plastic deformation. However, the case of thermodynamically stable NC alloys is even more special, requiring not simply the mixing of elemental species, but significant segregation at GBs.

Overall, GB segregation is difficult to obtain and control. Indeed, it is a spontaneous process that can be mostly induced, or favoured, only once the homogeneous solid solution of the two elemental metals has been fabricated. Further complications arise in the presence of immiscible elements, when thermal annealing intended to facilitate GB segregation can also result in demixing processes.

In the light of the considerations mentioned above, mechanical alloying (MA) methods appear particularly suited to the case. Nominally performed at low temperatures, they allow the efficient forced mixing of elemental metals, simultaneously refining the microstructure down to the nanometer range[108–110]. For this reason, we have chosen the MA by ball milling (BM) to fabricate the selected NC alloys.

Effectiveness of BM stems from the severe mechanical deformation imparted to powder particles by the impacts between milling tools, which are caused by the motion of the reactor

or of a part of it. At each impact, a fraction of the granular body inside the reactor gets trapped between the surfaces of the milling tools, thus undergoing severe mechanical load. The mechanical action is schematically depicted in Fig. 4.1a. Force chains develop along the network formed by the points of contact between neighbouring particles, finally resulting in plastic deformation, cold-welding and fracturing[108]. As results, a progressive refinement of the microstructure is achieved.

In fact, the repeated plastic deformation experienced by the processed powders can make the dispersion of two or more elemental metals so fine to result in their intimate mixing, which typically gives rise to the significant extension of solid solubility limits and the formation of NC or amorphous alloys.

While, MA was initially ascribed to local melting processes, it is now widely accepted that the thermally activated transport combines with the dislocation-mediated rearrangement of local structures and with the turbulent dynamics of atomic displacements at sheared interfaces[111–113]. Such behaviour can be appreciated from Fig. 4.1b. Here, scanning electron microscopy (SEM) images of a Nb_{50}-Ti_{50} mixture at early stages of MA are reported[114]. Elemental maps related to Nb (red dots) and Ti (green dots) highlight the typical lamellar structure observed during early stages of MA. The progressive homogenization of colour distribution reflects the progressive intermixing that is occurring as the MA proceeds up to 20 hours.

The level of microstructural refinement obtained during MA strictly depends on several variables such as the type of the mill, the material of milling media, the ball-to-powder ratio, the filling extent of the milling chamber, the milling atmosphere, the milling speed and the milling time[115]. Thus, an opportune selection of experimental conditions is fundamental to achieve the desired results.

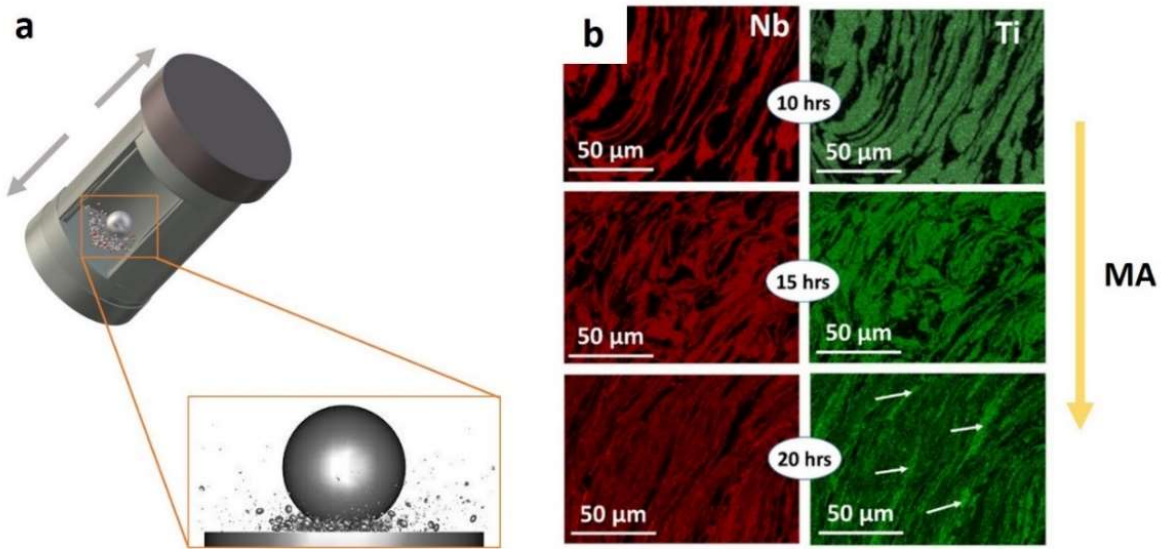

Fig. 4.1. (a) Schematic description of a collision during BM with a SPEX mill. **(b)** SEM electron dispersive spectroscopy (EDS) elemental maps for Nb and Ti after different milling times (the arrows identify pure Ti regions).[114]

4.2. Thermal stability of nanocrystalline metal alloys

As mentioned above, both nanostructure and fine mixing of components are necessary requirements in order to properly assess thermodynamic stability in NC alloy. Indeed, while the NC structure could represent in principle the most stable state, the achievement of the thermodynamic stability starting from a coarse-grained microstructure is quite improbable in the real systems. In fact, no evidences of a similar "from above" mechanism have been reported so far. Rather, the achievement of an equilibrium grain size is usually searched through a "from below" approach that starts from NC alloys. Nevertheless, an interplay between thermodynamic and kinetic stabilization mechanisms is observed also in this case, leading to several difficulties in the experimental assessment of thermodynamic stability.

At first glance, high temperatures and long annealing times can help to discriminate between kinetic and thermodynamic effects. Clearly, application of high temperatures may overcome kinetic barriers, as well as longer times allow materials to reach their preferred states. On the other hand, too high temperature treatments may lead to the underestimation

of thermodynamic effects when the results are interpreted in terms of materials structure stability. In fact, also the thermodynamic stable state is temperature dependent. Therefore, an increase of the grain size as the temperature is increased may be due to the overcome of kinetic barriers as well as to the change of thermodynamic stable state.

A possible compromise to evaluate competing kinetic factors, while limiting the time consumption, can be found in the approach reported by K.W. Liu and F. Mücklich for RuAl alloys[116]. They performed annealing experiments at different temperatures with increasing duration until reaching a steady state grain size.

The selection of the annealing temperatures represents a critical aspect and should be tuned on the specific system. In this sense, the melting point of the system has to be considered when evaluating the thermal stability.

W-Al alloys represent a particular case, as the melting point of Al is about 2700 °C lower than that of W. As result, a significant drop in the melting point of body-centred cubic (BCC) W-Al solid solution is observed as the amount of Al increases. Based on the phase diagram[117], homologous temperature

$$\Theta = \frac{T}{T_m} \tag{4.1}$$

can be evaluated. Here, T_m is the temperature at which melting of the bcc W(Al) solid solution begins, i.e. the solidus temperature, while T is the absolute temperature.

The Θ values corresponding to temperatures of 700 °C and 900 °C are reported in Table 1 for pure W and for different W-Al alloys. When annealed at 900 °C, W and $W_{80}Al_{20}$ experience homologous temperature of 0.32 and 0.79, respectively. These considerations were taken into account when designing the annealing experiments for W-Al alloys, as described in the experimental section of the present thesis.

Table 1. Homologous temperatures for W and W-Al systems at 700 °C and 900 °C.

	T_m [°C]	$\Theta_{700\,°C}$	$\Theta_{900\,°C}$
W	3422	0.26	0.32
W – 5 at.% Al	2587	0.34	0.41
W – 10 at.% Al	1657	0.50	0.61
W – 20 at.% Al	1207	0.66	0.79

5. Experimental

5.1. Mechanical alloying

We used a SPEX Mixer/Mill 8000 (SPEX CertiPrep, USA), to fabricate W-Al and W-Ag NC alloys starting from commercial high-purity powders.

For each run, 15 g of powders were sealed in a cylindrical reactor with three balls of 8 g. Both hardened steel and WC milling media were used. The amount of powders was large enough to ensure completely inelastic collisions between the grinding balls and the terminal walls of the reactor. Powders were handled inside a glove box under an inert Ar atmosphere with moisture and oxygen content below 5 ppm to avoid undesired oxidation processes. Mechanical treatments of increasing duration were then performed under Ar atmosphere. Experiments were periodically stopped to withdrawn small amounts of sample; this allowed monitoring the microstructure evolution during MA.

5.2. Annealing experiments

Annealing experiments were performed on NC alloys produced by BM at different temperatures using a vertical furnace under high vacuum conditions. Additional experiments were performed using a flowing Ar +3% H_2 mixture.

According with the considerations discussed in the previous chapter, each system was annealed at homologous temperature ranging from about 0.1 to about 0.8. However, in some cases very high or very low absolute temperatures would have been necessary in order to achieve high or low values of Θ. For instance, pure W should be annealed at 2737 °C in order to experience a homologous temperature of 0.8. For obvious reasons, annealing experiments could not be performed in similar cases. For a specific homologous temperature, samples were annealed for different times, ranging from 30 min to 36 h in order to better evaluate kinetic effects. To this aim, BM powders of W-Al were used. W-Ag alloys were also annealed because it is predicted to be unstable against phase separation. In this case, short annealing at 700 °C was sufficient to highlight phase separation in ball milled powders.

5.3. Sintering of powders

Spark plasma sintering (SPS) is a fast and simple way to obtain high density compacted starting from powders of a wide range of materials[118]. The schematic equipment of SPS process is shown in Fig. 5.1. The consolidation process happens due to the flow of an electrical current through the sample while an external load is applied. As result, the high heating rates up to 100 °C/min and the reduced thermal gradients characterizing SPS allow very short sintering times and lower temperature respect to conventional techniques.

W-Al powders obtained by MA were consolidated using an SPS 515 Sumitomo CoalMining Co Ltd apparatus. About 4 g of powders were put inside a cylindrical graphite die with internal diameter 10 mm, and symmetrically closed with plungers 22 mm in high and 9.5 mm in diameter. Densification was performed at 1000 °C and 1100 °C using a heating rate of 100 °C/min and maintaining the reached temperature for 30 min. During the heating, the applied mechanical load was gradually increased until 6.3 kN and kept constant for all the isothermal step, ensuring a pressure of around 80 MPa.

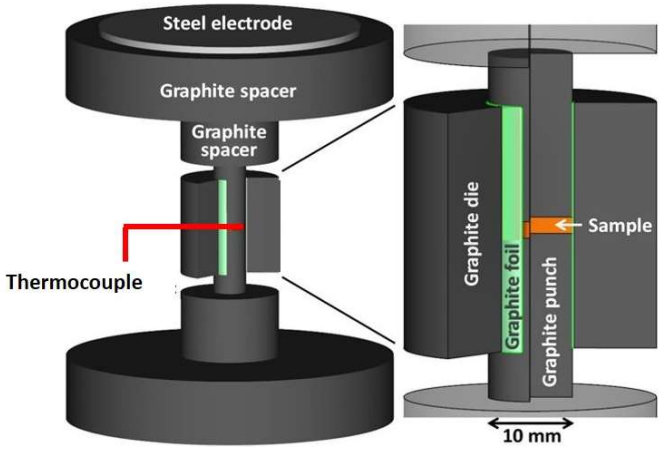

Fig. 5.1. A schematic view of the SPS apparatus.

Pressureless experiments were also performed under flux of Ar + 3% H_2 using a thermomechanical analyzer (TMA) from Netzsch Instruments, starting from cold-pressed

disks with radius and thickness of 3 mm and 1.5 mm, respectively. This allowed to measure *in situ* length changes.

5.4. Characterization methods

5.4.1. X-ray diffraction

X-ray diffraction (XRD) is a relatively fast and simple analytical technique that is widely used for the characterization of solids with a certain degree of crystallinity. When applied to powders, it allows to characterize a representative amount of the sample and to obtain qualitative and quantitative information concerning the crystallographic phases present and their microstructure[119]. In this regard, the analysis of XRD patterns according with the Rietveld method[120] indirectly allows estimating averages quantities as the coherent diffraction domain, lattice microstrain and lattice parameters. For these reasons, X-ray diffraction is widely applied to the study of NC alloys.

Microstructural evolution of powders during MA, as well as after annealing and sintering experiments was followed using a Rigaku Miniflex II diffractometer equipped with Cu Kα radiation (λ=1.5405 Å). XRD patterns were collected over a scattering angle range from 10 to 140°. The obtained XRD patterns were analyzed according with the Rietveld method using the Maud software[121].

5.4.2. Scanning electron microscopy

A SEM-EDS Zeiss Evo LS15 microscopy equipped with a LaB_6 crystal as electron source was used to investigate the morphology and cross section of BM powders. The cross-section of sintered samples was investigated using FEG-SEM (Zeiss LEO 35) equipped with backscattered electron detector and microanalysis for Energy Dispersive X-ray analysis (EDS).

5.4.3. Transmission electron microscopy

Micrographs and chemical maps were obtained using a state of the art JEOL ARM 200F (STEM) and FEI Titan3 (TEM and STEM) electron microscopes equipped with a probe and image aberration corrector and operating in mode at 200 kV and 300 kV acceleration voltage respectively. A Thermo Scientific (make, model, area + quadra in Titan) EDS detector was used for the acquisition of chemical maps which were summed over 100 frames for the improvement of the signal to noise ratio (SNR). Selected area electron diffraction (SAED) were performed.

5.4.4. Differential scanning calorimetry

Differential scanning calorimetry (DSC) is a technique in which the heat of flux (power) to the sample is monitored against time or temperature, while the temperature of the sample is programmed. The difference in heat flux respect to a reference is monitored, giving information about endothermic or exothermic processes occurring in the sample. For a certain process, the change in the enthalpy is obtained by integrating the related peak in the heat flow profile. In some cases, kinetic information can also be obtained[122].

When applied to NC alloys, DSC allows highlighting different types of transformations such as the formation of intermetallic compounds, polymorphic transitions, crystallization and melting processes. Due also to the small amount of sample required, this technique is commonly used to study the thermal stability.

In the present work, a Star System TGA/DSC by Mettler-Toledo was used to analyse the powder samples. About 1.3 mg of powders were sealed in an alumina crucible. Before each run, a blank measurement was performed. To this aim, the empty crucible was heated up according with the same heating program that was subsequently used to analyse the sample. In this way, artefacts related to the instrument or to the crucible were opportunely subtracted.

6. Results and discussion

The mechanical processing by BM induces a significant microstructural evolution of both W-Ag and W-Al powder mixtures. The former, which is predicted to be thermally unstable and prone to phase separation, exhibits a MA behaviour different from the W-Al mixture, which is, instead, a promising candidate for thermodynamic stabilization. However, a careful characterization was required to properly evaluate the thermodynamic stability of the two binary alloys.

For clarity, the two experimental case studies are discussed separately in the following.

6.1. W-Ag system

6.1.1. Kinetics of MA

XRD patterns shown in Fig. 6.1 describe the microstructural evolution of $W_{85}Ag_{15}$ mixtures under mechanical processing conditions. Bragg peaks related to both BCC W and face-centred cubic (FCC) Ag show a progressive broadening, along with a decrease of the intensity. This definitely indicates that BM induces a significant microstructural refinement[108]. Nevertheless, it does not result in the complete dissolution of Ag in the W lattice. Indeed, the Bragg peaks of FCC Ag were detected even after 100 h. This can be clearly seen in Fig. 6.1b, where the best fitted Rietveld profile and the individual phase contributions are shown. An amorphous phase seems to form already after 62 h of MA.

Average grain sizes of about 15 and 10 nm were obtained for BCC W(Ag) and FCC Ag(W) solid solutions respectively. These values are in agreement with those reported in the literature for a W-25 wt.% Ag NC composite subjected to 110 h of BM[123].

The incapability of obtaining a homogeneous solid solution can be ascribed to the marked differences between Ag and W in terms of mechanical properties. While the former has a shear modulus of 30 GPa, it is of 160 GPa for the latter. Similarly, the hardness is equal to 0.25 GPa for Ag, while it is around 3.5 GPa for W. Such differences unavoidably lead to

localized plastic flow in the Ag phase, leaving W almost unaffected. As expected[124,125], any mixing process on the atomic scale is hindered.

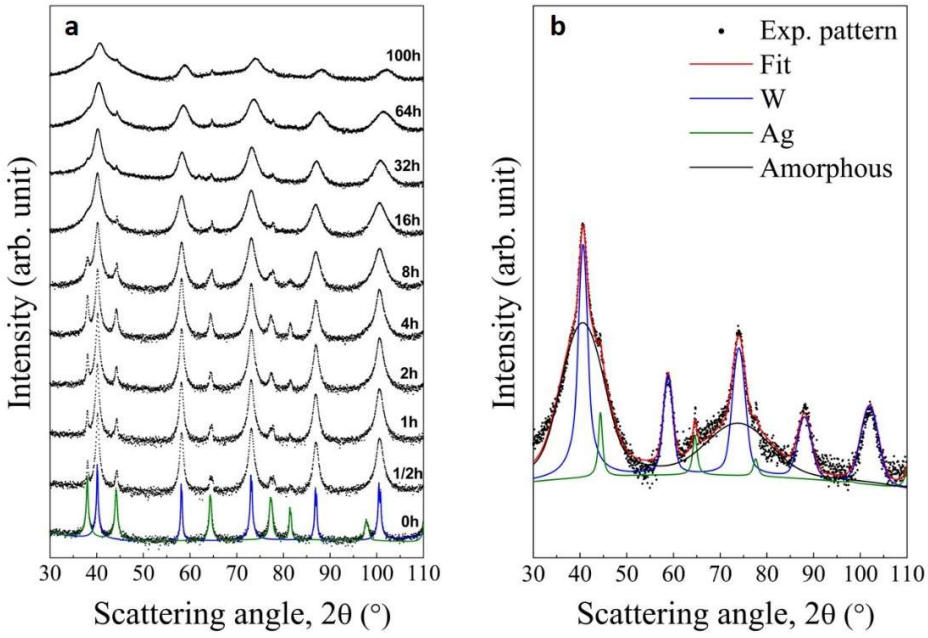

Fig. 6.1. (a) XRD patterns of $W_{85}Ag_{15}$ mixtures at increasing MA times. **(b)** XRD pattern of the sample processed for 100 h. The best-fitted Rietveld profiles for the different phases are shown.

Thermodynamic factors can also be at work. In particular, the high positive enthalpy of mixing of W-Ag, equal to about 40 kJ/mol at the equiatomic composition[107], can prevent any mutual dissolution at the nanometer scale[126,127], giving also rise to chemical bias during forced mixing processes induced by shearing[128].

6.1.2. Thermal instability of $W_{85}Ag_{15}$ mixtures

$W_{85}Ag_{15}$ mixtures processed for 100 h were subjected to thermal annealing to evaluate the thermal stability of the nanostructure. As expected, phase separation of FCC Ag was observed after annealing at relatively low temperatures. XRD patterns in Fig. 6.2 clearly show that even short annealing at 700 °C induces a significant reduction of the amorphous

fraction and makes Bragg peaks characteristic of the FCC Ag phase appear. The same phase separation behaviour takes place at 800 °C.

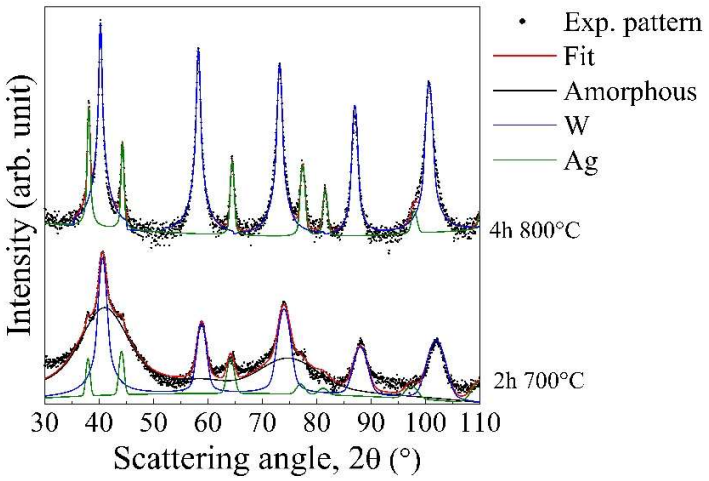

Fig. 6.2. XRD pattern of $W_{85}Ag_{15}$ mixtures after 100 h of BM and subsequent annealing at 700 °C for 2 h and at 800 °C for 4 h.

Thus, experimental evidence on W-Ag seems to support the model prediction. Indeed, the two-phase state seems to represent the thermodynamically favoured state.

6.2. W-Al system

6.2.1. Kinetics of MA

Binary W-Al alloys with Al content ranging from 5 to 20 at.% of Al were fabricated by MA. Representative XRD patterns of $W_{80}Al_{20}$ are shown in Fig. 6.3 for illustrative purposes. The Bragg peaks of the BCC phase progressively broaden under the effects of mechanical processing. No amorphisation is observed in this case. Only a BCC solid solution is detected. Regardless the chemical composition, a final average grain size of about 10 to 15 nm was obtained.

The Bragg peaks of FCC Al disappeared already during the early stages of MA. In principle, this could suggest the complete Al dissolution as observed in the literature for an equiatomic W-Al solid solution.[129] Nevertheless, XRD is unable to detect small fractions of dispersed phases formed by light elements. Moreover, absorption phenomena due to the heavy W and lattice disorder further complicate the analysis.

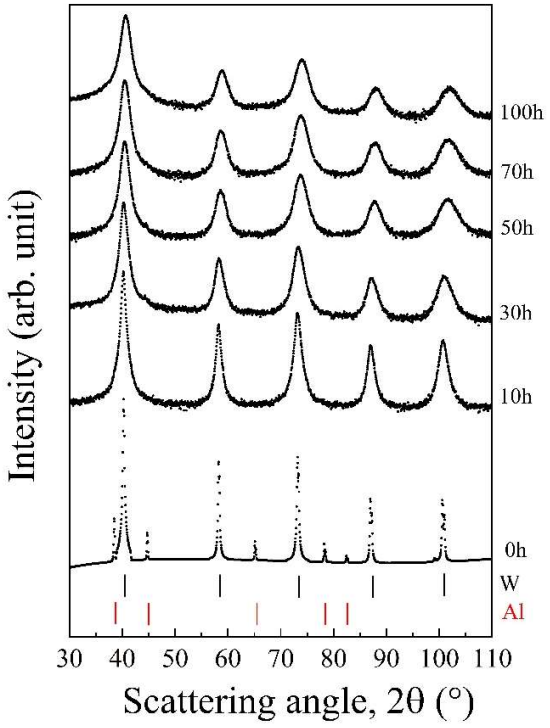

Fig. 6.3. XRD patterns of $W_{80}Al_{20}$ mixtures at increasing MA time.

Valuable evidence in this respect was obtained by SEM and TEM observation. A representative SEM micrograph of $W_{20}Al_{80}$ powder processed for 100 h is shown in Fig. 6.4a. The homogeneous microstructure suggests a high degree of intermixing. This finds support in the EDS analysis, which indicates an average chemical composition in line with expectations. TEM provided clear evidence that BM induces high microstructural refinement. The TEM micrograph shown in Fig. 6.4b indicates that the average grain size of $W_{20}Al_{80}$ processed for 100 h is around 12 nm, in fairly good agreement with the Rietveld estimate.

SAED in Fig. 6.4b assigns the (211), (200) and (110) reflections characteristic of the BCC W. No diffraction spot can be ascribed to the FCC Al, thus confirming that W(Al) solid solution is the only phase present after MA. This marks a significant difference with respect to the W-Ag case. Indeed, a single intermixed phase is obtained despite the large differences between Al and W in terms of mechanical properties, with Al exhibiting shear modulus and hardness around 30 GPa and 0.17 respectively. It follows that the formation of the solid solution has been somehow favoured by chemical effects.

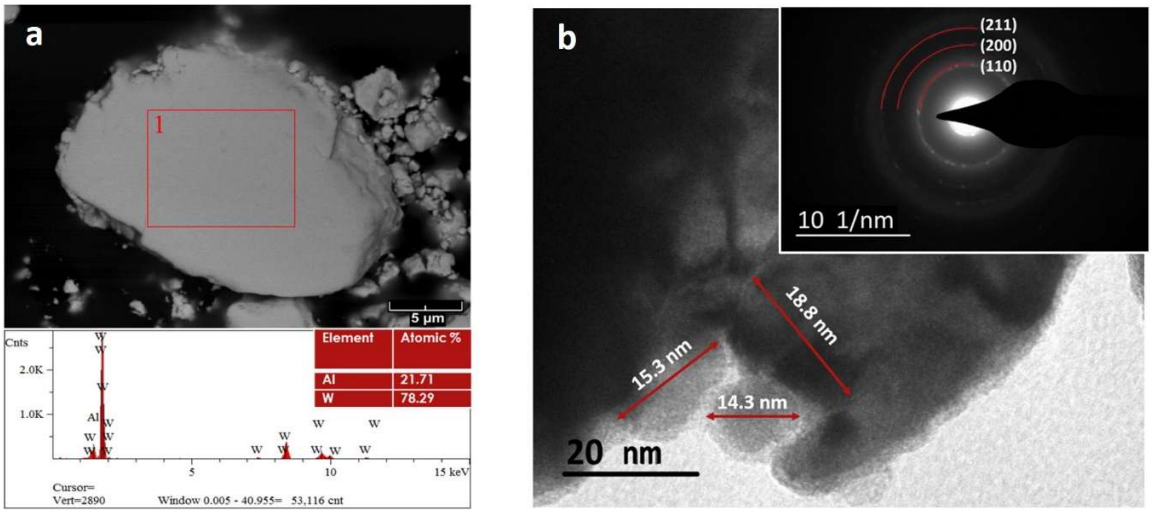

Fig. 6.4. (a) Cross-section back scattering SEM image of a $W_{80}Al_{20}$ particle after 100h of MA. EDS chemical analysis of the selected area is also reported. **(b)** TEM micrographs and *in situ* electron diffraction of a $W_{80}Al_{20}$ particle after 100 h of BM.

6.2.2. Thermal stability of W-Al mixtures

The DSC analysis of NC W-Al alloys during heating up to 1450 °C provides a first indication of thermal stability. Heat flow profiles obtained for $W_{90}Al_{10}$ and $W_{80}Al_{20}$ NC solid solutions are shown in Fig. 6.5. The profile of the blank sample is also shown in Fig. 6.5a. Top and bottom curves refer to the heating and cooling stages respectively.

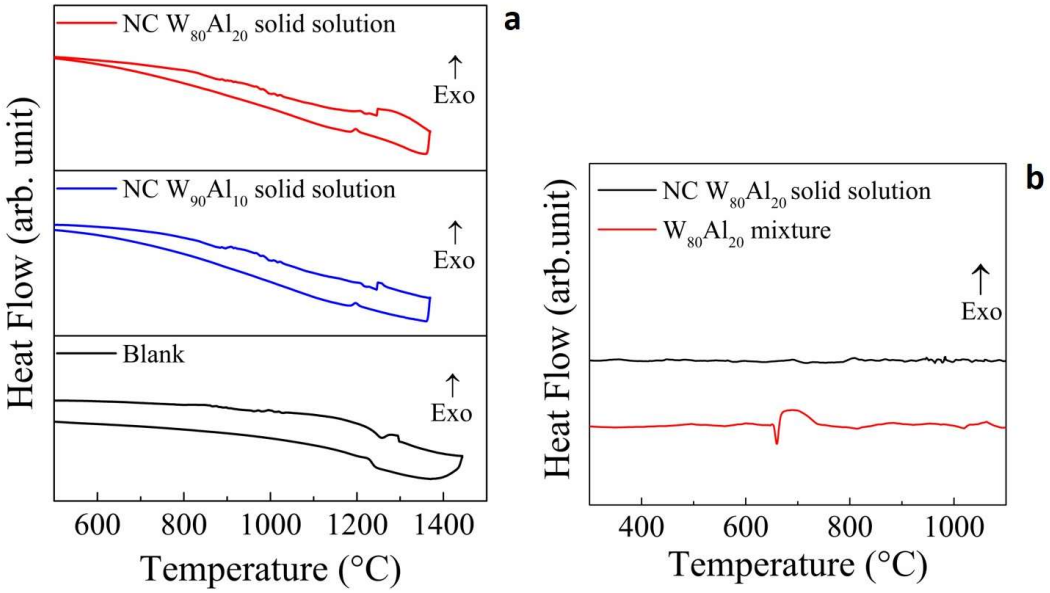

Fig. 6.5. DSC profiles of NC W-Al alloys. **(a)** Heating and cooling profiles of NC $W_{80}Al_{20}$ and $W_{90}Al_{10}$ acquired up to 1450 °C are compared with the blank. **(b)** Heating profile of a $W_{80}Al_{20}$ mixture of commercial powders compared with that of NC $W_{80}Al_{20}$ alloy.

The DSC curves of the two NC alloys and of the blank sample exhibit small fluctuations in the temperature range between 1250 °C and 1300 °C. Therefore, they can be ascribed to instrumental factors. No evidence of Al melting is detected. This strongly suggests that no elemental Al phase is present. Rather, it must be reasonably expected that Al is dissolved in W. A mixture of unalloyed W and Al commercial powders with the same stoichiometry was also analysed for comparison. As expected, Al melting is readily observed, marked by the endothermic peak at 660 °C in Fig. 6.5b. The Al melting peak is immediately followed by an exothermal event, indicated by the broad peak between 670 °C and 735 °C. According to literature[130], it is related to the formation of WAl_4 and WAl_5 intermetallic compounds. XRD patterns confirm the formation of the intermetallic phases, as shown in Fig. 6.6.

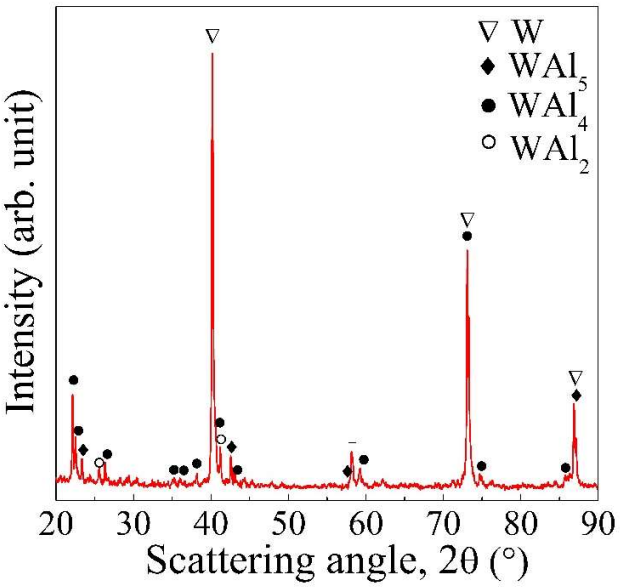

Fig. 6.6. XRD pattern of the $W_{80}Al_{20}$ unalloyed mixture annealed at 1450 °C.

It is worth noting that no intermetallic phase was detected in XRD patterns of the annealed NC alloys, which are shown in Fig. 6.7. Except for WC contamination coming from milling tools (around 3-4 wt.%), only the BCC W(Al) is detected. This is still in agreement with the model predictions. Indeed, the ordered WAl_4 compound is predicted to not affect the stability of NC W-Al alloys.

It is also worth noting that both NC $W_{80}Al_{20}$ and NC $W_{90}Al_{10}$ heated up to 1450 °C show averages grain size of about 70 and 60 nm respectively. In contrast, pure NC W undergoes rapid grain growth and reaches average grain size of about 2 μm.

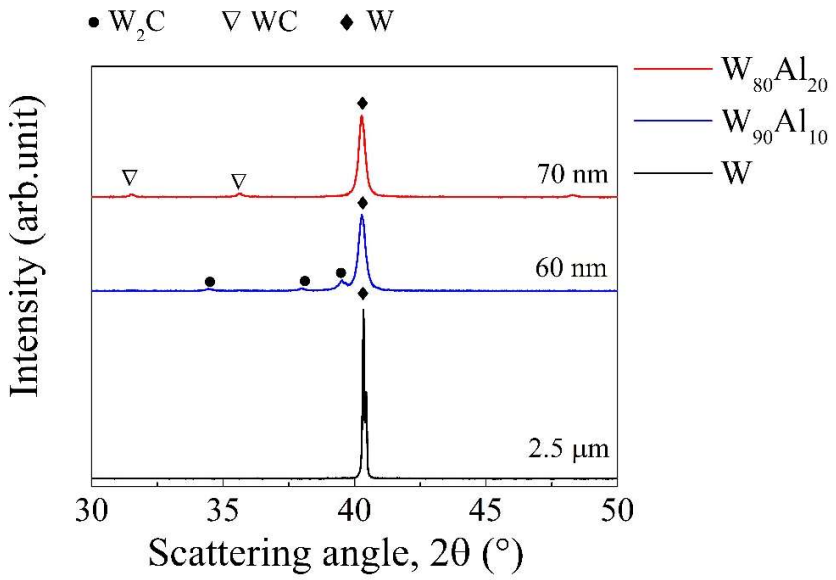

Fig. 6.7. XRD patterns of NC W, $W_{90}Al_{10}$ $W_{80}Al_{20}$ annealed at 1450 °C.

The thermal stability of NC W-Al mixtures was further investigated by performing kinetic analyses of grain growth at constant temperature. Data are shown in Fig. 6.8, where the equilibrium grain size attained after annealing is plotted for alloys of different chemical composition as a function of homologous temperature. Depending on the temperature and on the composition, the time required to reach a plateau condition varied from 12 to 36 h.

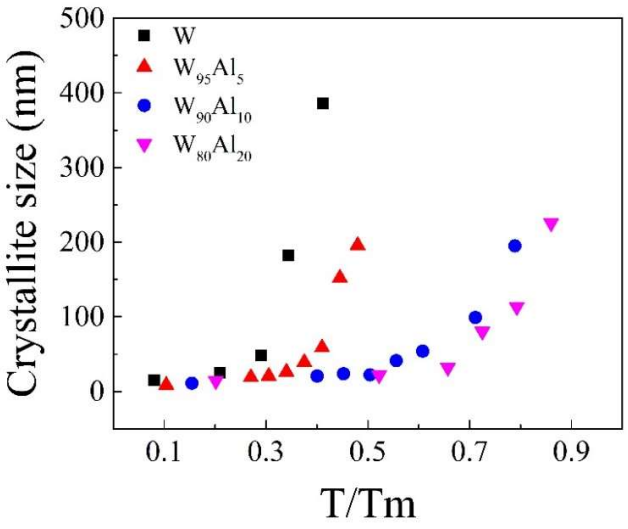

Fig. 6.8. Equilibrium grain size reached by W-Al alloys with different chemical composition at increasing homologous temperatures. Values obtained for W are also shown for comparison.

Despite a rapid grain growth can be expected, elemental NC W is relatively stable at low homologous temperatures. Kinetic factors due to impurities, e.g. contaminating elements from milling tools, can explain the apparent stability. As the homologous temperature increases from 0.3 to about 0.35, a significant grain growth up to about 400 nm takes place. Better performances are observed in the $W_{95}Al_5$ case, which retains its nanostructure at homologous temperatures up to about 0.4. Along the same line, NC $W_{90}Al_{10}$ and NC $W_{80}Al_{20}$ alloys exhibit significant stability even at homologous temperatures of 0.7 and 0.8 respectively. This provides an additional, positive indication that experimental evidence agrees with model prediction (see paragraph 3.2.3).

NC W and W-Al powders obtained by MA were consolidated to better investigate thermal effects on microstructural evolution. A representative TEM micrograph of a $W_{80}Al_{20}$ sample sintered at 1000 °C is shown in Fig. 6.9 together with the chemical mapping. In agreement with the Rietveld analysis, grain size is about 100 nm or less. Chemical mapping indicates a homogeneous dispersion of Al in W. Fe and Co impurities (3 and 2 wt.% respectively) are also observed, due to contamination from the milling media, and tends to form separate domains, i.e. large dark areas in Fig.6.9.

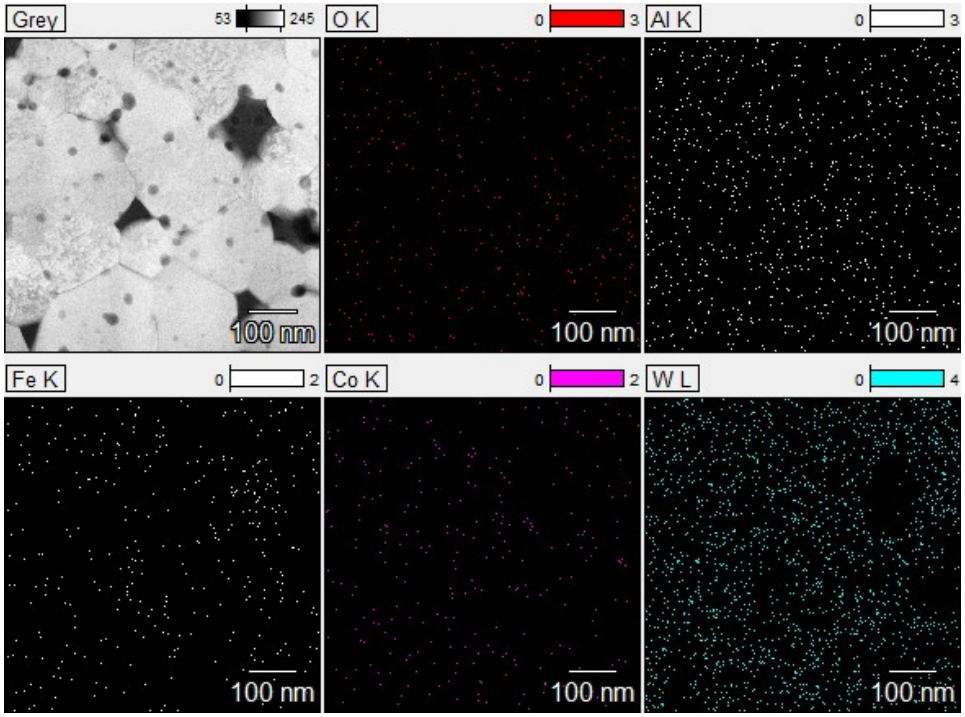

Fig. 6.9. TEM image and chemical mapping of a $W_{80}Al_{20}$ sample sintered at 1000 °C.

The TEM micrograph of the consolidated sample shows also smaller dark areas preferentially located at GBs. High resolution TEM provides more details in this regard. For instance, the detail image in Fig. 6.10 shows the nanostructure of a large island located at the boundary between three W grains. First, it is worth noting that dark regions are not rich in Fe. Rather, the chemical map indicates that W and Al are present in ratio 1:1. This means that Al content is significantly higher at GBs with respect to the typical grains characterized by a 4:1 W:Al ratio.

Moreover, Al-segregated regions are located near GBs characterized by a high density of defects and lattice disorder. This provides some support to the hypothesis that the release of elastic strain can be a driving force for solute segregation at GBs. Finally, the formation of W-Al intermetallic compounds is definitely ruled out. SAED of segregated regions, which can be found at the bottom right corner of Fig. 6.10, reveals only reflection planes characteristic of the BCC lattice. Furthermore, lattice parameters near GBs are slightly larger

with respect to those observed in the grain interior. Such volume increase of W lattice can be reasonably ascribed to the higher concentration of Al atoms, which have bigger atomic volume than W.

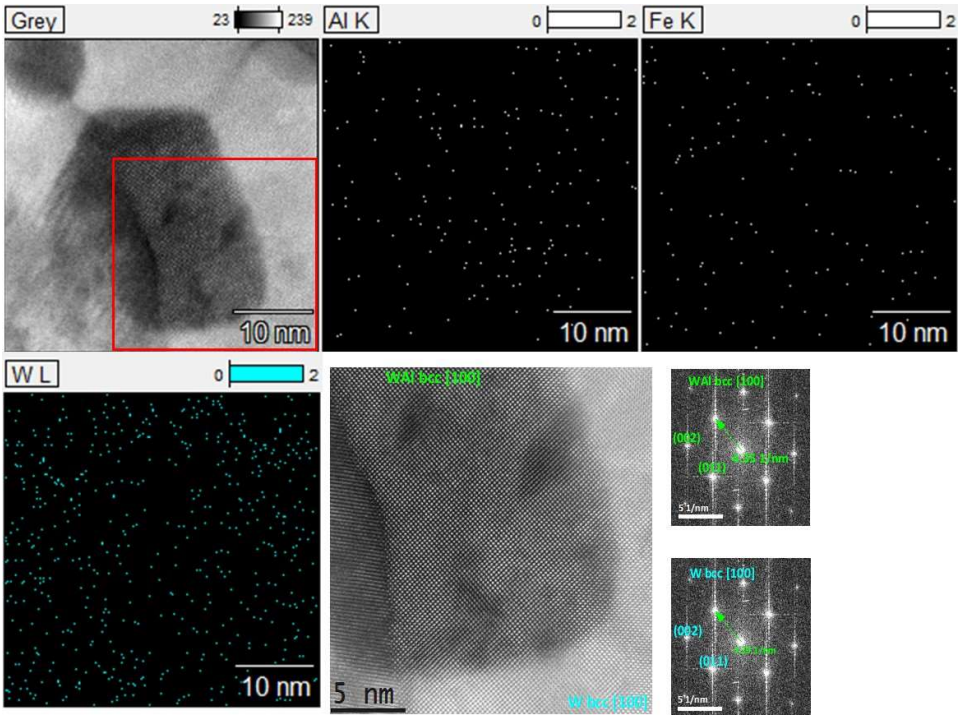

Fig. 6.10. High-resolution TEM and chemical maps of an Al-rich area located at a triple junction.

Overall, our results are in line with model predictions and suggest that, despite the simplifying assumptions, the developed thermodynamic framework can be used to identify potential candidates for stable NC alloys. In particular, experimental evidences on the W-Al system demonstrate that GB segregation can result in the thermal stability also for NC binary alloys characterized by a negative enthalpy of mixing. Despite kinetic contributions to such stabilization cannot completely be ruled out, a significant effort to minimize their effects has been made by adopting the experimental methodology that has been previously described in detail. Thus, experimental evidences indicate that thermodynamics must play, at least, a fundamental role in the thermal stability of the W-Al system by drastically reducing the driving force for both grain growth and second phase precipitation.

7. Conclusions

The present thesis illustrates part of the experimental investigations at the cutting edge of research fields in Materials Science and in general Physical Metallurgy in particular. Aiming at the design and fabrication of multicomponent, multiphase thermodynamically stable NC metal alloys, current studies address the unprecedented challenge of revolutionizing one of the most intensely explored areas of investigations in Materials Science, namely the one related to nanostructured metals.

To such aim, the present thesis combines theoretical modelling and experimental validation. Based on the hypothesis that solute segregation at GBs can result in a significantly enhanced thermal stability of NC alloys, we developed a model that describes the thermodynamics of NC metal alloys involving an arbitrary number of elemental constituents and phases. The general model allows for the inhomogeneous partition of solutes within the microstructure consisting of crystalline grains and GBs belonging to different phases. Despite ordered compounds are not directly considered in the mathematical formalism, they can be subsequently included in the equilibrium phase diagrams. This avoid adding unnecessary complexity to the model. At the same time, it permits to evaluate whether intermetallics formation could or not affect the thermodynamic stability of the NC solid solutions. State variables and energetic parameters describing interatomic interactions within grains and at GBs determine the shape of the Gibbs free energy surface of the NC metal alloy in a multidimensional parameter space. The exploration of the obtained Gibbs free energy surface in search of local and global minima represents the most reliable method to evaluate the contribution of GB solute segregation to the system thermodynamics.

We examined the possible attainment of structural stability due to GB segregation within the framework of equilibrium thermodynamics. Binary and ternary metal alloys have been systematically investigated to identify candidate systems possibly able to exhibit thermodynamic stability under suitable thermal and microstructural conditions.

Our interest focused on W-based alloys because of the availability of energetic parameter values and because of the experimental evidence suggesting that a few W-based alloys are thermodynamically stable. In this respect, we extended investigations to miscible binary

alloys such as W-Al ones and checked the model validity against W-Ag, predicted to exhibit a strong tendency to phase separation.

Differences between W-Al and W-Ag alloys emerge clearly. While homogeneous NC W-Al alloys were easily obtained by MA of elemental powders, W-Ag mixtures keep a segregated structure on relatively coarse length scales. Annealing at relatively low temperature readily induces the formation of large W and Ag domains, whereas W-Al mixtures showed a significant thermal stability even at high homologous temperatures. In addition, the annealing of W-Al alloys does not result in the formation of intermetallic compounds in agreement with model predictions regarding the ordered WAl_4 intermetallic.

Concerning W-Al alloys, TEM observation of samples annealed at 1000 °C definitely show the marked tendency of Al to segregate at GBs. This provides significant support to the hypothesis that solute segregation at GBs can stabilize the nanostructure even in binary alloys formed by elements that exhibit a negative enthalpy of mixing. In this regard, despite kinetic contributions cannot completely be ruled out, their effect have been tentatively minimized.

Overall, the experimental findings emphasize the potential of the thermodynamic modelling developed in the design of NC metal alloys with enhanced coarsening resistance. It definitely appears that the intrinsic microstructural instability related to the high volume density of GBs can be significantly reduced, or suppressed, in the presence of alloying element able to segregate at GBs. While the favourable influence of GB segregation has been proven so far only for immiscible alloys, we have shown that similar effects can be expected for miscible alloys.

It is reasonable to think that the model developed will be able to account for the thermodynamic behaviour of practical case studies more complicated than binary alloys. It is exactly towards multicomponent metal alloys that the most advanced studies in the field are currently oriented. However, this model only represents a first effort towards this ambitious achievement. Further improvements, as for instance the introduction of liquid phases, are required in order to better describe the thermodynamics of real systems. At the same time, the increasing scientific interest on this topic may soon lead to significant improvements in the calculation/ or estimation of parameters related to GBs, which have been shown to deeply affect the reliability of the model predictions.

Acknowledgements

First and foremost, I would like to express my gratitude to Prof. Francesco Delogu and Prof. Antonio Mario Locci for their kind support and all the knowledge they taught me.

I would like to thank also Prof. Cao and Prof. Orrù for giving me the opportunity to perform my research activity in the framework of the international PhD in Innovation Sciences and Technologies at the University of Cagliari.

I gratefully acknowledge Sardinian Regional Government for the financial support of my PhD scholarship (P.O.R. Sardegna F.S.E. - Operational Programme of the Autonomous Region of Sardinia, European Social Fund 2014-2020 - Axis III Education and training, Thematic goal 10, Investment Priority 10ii), Specific goal 10.5.

I am grateful to the Future and Emerging Technologies programme of the Horizon 2020 platform and to the Cost action "Solutions for Critical Raw Materials Under Extreme Conditions" for the financial support during the conferences and the schools I have attended to.

During my Ph.D. I had the chance to collaborate with different research groups.

In this regard, I am grateful to Prof. Tomas Polcar and Prof. Yi Huang for their kind hospitality during my stay at the University of Southampton. Many thanks to Deepack Kumar Ranga for his constant technical advices and to Teodor Huminiuc for TEM characterizations.

I would like to thank Prof. Christopher A. Schuh for giving me the opportunity to perform part of my Ph.D. activity at the Massachusetts Institute of Technology. Thanks to the Schuh group for both serious and fun office discussions and for their help in the lab.

Many thanks also to Dr. Antonio Rinaldi and Dr. Claudio Mingazzini from ENEA for the characterizations performed.

I gratefully acknowledge Sebastiano Garroni for his technical advices and for the help with experimental activity.

I am grateful to Prof. Roberta Licheri, Prof. Paola Meloni, Dr. Elodia Musu, Dr. Barbara Lasio, Dr. Gianfranco Carcangiu, Dr. Giorgio Pia, Dr. Luca Pilia and Dr. Giorgio Ligios for their help during my research activity.

Thanks to Siul, Callum, Nico, Dan, Megan, Robbie, Simon, Deepack, Sebastian and all the people for the great time in Southampton. Hope to see you soon.

Thanks to Martina, Agnese, Simone, Mim, the two Fabio, Paolo, Gianpaolo, Lucrezia, Ilaria, Gorgia, Tejas, Basuhi, and all the MIT crew. I left parts of my heart on the other side of the ocean.

Thanks to Claudio, Paolo, Marina, Giovanna, Gabriele, Fabio, Sara, Pablo, Elisa, Alessandra, Blessing, Roberto, Alessandro and all the colleagues for the shared lunches, coffees, anxieties and countless laughs. Suffering the pains of a Ph.D. has been pleasant with you around.

Thanks to the girls of via Donizetti, my second family during these three years.

Finally, I would like to thanks my lifelong friends, Silvia and my family for their lovely support. I am blessed to have you in my life.

References

1. Report, S. & Academy, N. *Materials and Man's Needs: Materials Science and Engineering*. *Materials and Man's Needs* (National Academies Press, 1975).
2. Washburn, S. *Speculations on the interrelations of the history of tools and biological evolution*. **31**, (Wayne State University Pree, 1959).
3. Brues, A. The Spearman and the Archer - An Essay on Selection in Body Build. *Am. Anthropol.* **61**, 457–469 (1959).
4. Wertime, T. A. Man's First Encounters with Metallurgy. *Science (80-.).* **146**, 1257–1267 (1964).
5. National Research Council. *Minerals, Critical Minerals, and the U.S. Economy*. *Minerals, Critical Minerals, and the U.S. Economy* (2015).
6. W. Cahn. *The Coming of Materials Science*. (Elsevier Science Ltd, 2001).
7. Olson, G. Designing a New Material World. *Science (80-.).* **288**, 993–998 (2000).
8. Bederson, B. *A celebration of Physics at the Millennium*. (Springer-Verlag Berlin Heidelberg, 1999).
9. https://downloadfiles.grantadesign.com/pdf/teaching_resource_books/2-Materials-Charts-2010.pdf. 5 (2010).
10. Saito, T. *Computational Materials Design*. (Springer-Verlag Berlin Heidelberg GmbH, 1999).
11. Gleiter, H. Nanocrystalline materials. *Prog. Mater. Sci.* **33**, 223–315 (1989).
12. Suryanarayana, C. & Kock, C. C. Nanocrystalline materials – Current research and future directions. *Hyperfine Interact.* **130**, 5–44 (2000).
13. Gusev, A. I. & Rempel, A. *Nanocrystalline Materials*. (Cambridge International Science Publishing, 2004).

14. Eftekhari, A. *Nanostructured Materials in Electrochemistry*. (Wiley-VCH, 2008).

15. Gilroy, K. D., Ruditskiy, A., Peng, H. C., Qin, D. & Xia, Y. Bimetallic nanocrystals: Syntheses, properties, and applications. *Chem. Rev.* **116**, 10414–10472 (2016).

16. Whang, S. H. *Nanostructured metals and alloys*. (Woodhead Publishing Limited, 2011).

17. Lu, L., Shen, Y., Chen, X., Qian, L. & Lu, K. Ultrahigh Strength and High Electrical Conductivity in Copper. *Science (80-.).* **304**, 422–427 (2004).

18. Erb, U., Aust, K. T. & Palumbo, G. Electrodeposited Nanocrystalline Metals, Alloys, and Composites. in *Nanostructured Materials: Processing, Properties, and Applications: Second Edition* 235–292 (Elsevier Inc., 2006). doi:10.1016/B978-081551534-0.50008-7

19. El-Atwani, O. *et al.* In-situ TEM observation of the response of ultrafine- and nanocrystalline-grained tungsten to extreme irradiation environments. *Sci. Rep.* **4**, 4–10 (2014).

20. Kumpmann, A., Günther, B. & Kunze, H. D. Thermal stability of ultrafine-grained metals and alloys. *Mater. Sci. Eng. A* **168**, 165–169 (1993).

21. Pantleon, K. & Somers, M. A. J. Interpretation of microstructure evolution during self-annealing and thermal annealing of nanocrystalline electrodeposits-A comparative study. *Mater. Sci. Eng. A* **528**, 65–71 (2010).

22. Westerdal, M., Rights, A. & Copyright, I. On the room-temperature grain growth in nanocrystalline copper. **30**, 577–581 (1994).

23. Ames, M. *et al.* Unraveling the nature of room temperature grain growth in nanocrystalline materials. *Acta Mater.* **56**, 4255–4266 (2008).

24. Natter, H., Schmelzer, M. & Hempelmann, R. Nanocrystalline nickel and nickel-copper alloys: Synthesis, characterization, and thermal stability. *J. Mater. Res.* **13**, 1186–1197 (1998).

25. Detor, A. J. & Schuh, C. A. Microstructural evolution during the heat treatment of

nanocrystalline alloys. *J. Mater. Res.* **22**, 3233–3248 (2007).

26. Kapoor, M., Kaub, T., Darling, K. A., Boyce, B. L. & Thompson, G. B. An atom probe study on Nb solute partitioning and nanocrystalline grain stabilization in mechanically alloyed Cu-Nb. *Acta Mater.* **126**, 564–575 (2017).

27. Lu, P. *et al.* On the thermal stability and grain boundary segregation in nanocrystalline PtAu alloys. *Materialia* **6**, (2019).

28. Tang, F. *et al.* Solute segregation and thermal stability of nanocrystalline solid solution systems. *Nanoscale* **11**, 1813–1816 (2019).

29. Marvel, C. J., Hornbuckle, B. C., Darling, K. A. & Harmer, M. P. Intentional and unintentional elemental segregation to grain boundaries in a Ni-rich nanocrystalline alloy. *J. Mater. Sci.* **54**, 3496–3508 (2019).

30. Fan, Z. *et al.* In situ studies on superior thermal stability of bulk FeZr nanocomposites. *Acta Mater.* **101**, 125–135 (2015).

31. Cai, X. C. *et al.* Selection of grain-boundary segregation elements for achieving stable and strong nanocrystalline Mg. *Mater. Sci. Eng. A* **717**, 144–153 (2018).

32. Chookajorn, T., Murdoch, H. A. & Schuh, C. A. Design of stable nanocrystalline alloys. *Science (80-.).* **337**, 951–954 (2012).

33. Rollett, A., Humphreys, F., Rohrer, G. S. & Hatherly, M. *Recrystallization and Related Annealing Phenomena: Second Edition*. (Pergamon, 2004).

34. Weissmüller, J. Alloy Effects in Nanostructures. *Nanostructured Mater.* **3**, 261–272 (1993).

35. https://www.mgi.gov/activities.

36. https://www.nsf.gov/.

37. https://icarus-alloys.eu/project.

38. http://metallographic.com/Consumables/Metallography-Intro.html.

39. https://www.fei.com/image-gallery/grain-boundary-gold/.

40. Shi-Hao, L., Jing-Ting, L. & Wei-Zhong, H. Radiation-Induced Helium Bubbles in Metals. *Materials (Basel).* **12**, 1036 (2019).

41. Haber, J. A. & Buhro, W. E. Kinetic instability of nanocrystalline aluminum prepared by chemical synthesis; facile room-temperature grain growth. *J. Am. Chem. Soc.* **120**, 10847–10855 (1998).

42. Klement, U., Erb, U., El-Sherik, A. M. & Aust, K. T. Thermal stability of nanocrystalline Ni. *Mater. Sci. Eng.* **A203**, 177–186 (1995).

43. Burke, J. E. & Turnbull, D. Recrystallization and grain growth. *Prog. Met. Phys.* **3**, (1952).

44. Peng, H. R., Gong, M. M., Chen, Y. Z. & Liu, F. Thermal stability of nanocrystalline materials: thermodynamics and kinetics. *Int. Mater. Rev.* **62**, 303–333 (2017).

45. Xu, D., Ji, C., Zhao, H., Ju, D. & Zhu, M. A new study on the growth behavior of austenite grains during heating processes. *Sci. Rep.* **7**, 3968 (2017).

46. Jansohn, P. *Modern gas turbine systems*. *Modern gas turbine systems* (Woodhead Publishing Series in Energy, 2013).

47. Koch, C. C., Scattergood, R. O., Darling, K. A. & Semones, J. E. Stabilization of nanocrystalline grain sizes by solute additions. *J. Mater. Sci.* **43**, 7264–7272 (2008).

48. Amram, D. & Schuh, C. A. Interplay between thermodynamic and kinetic stabilization mechanisms in nanocrystalline Fe-Mg alloys. *Acta Mater.* (2018).

49. Divinski, S. V., Reglitz, G., Wegner, M., Peterlechner, M. & Wilde, G. Effect of pinning by an orientation gradient on the thermal stability of ultrafine grained Ni produced by equal channel angular pressing. *J. Appl. Phys.* (2014).

50. Michels, A., Krill, C. E., Ehrhardt, H., Birringer, R. & Wu, D. T. Modelling the influence of grain-size-dependent solute drag on the kinetics of grain growth in nanocrystalline materials. *Acta Mater.* (1999).

51. Bansal, C., Gao, Z. Q. & Fultz, B. Grain growth and chemical ordering in (Fe,Mn)3Si. *Nanostructured Mater.* (1995).

52. Sikdar, K., Mahata, A., Roy, B. & Roy, D. Hybrid thermal stabilization of Zr doped nanocrystalline Cu. *Mater. Des.* (2019).

53. Liu, F. & Kirchheim, R. Grain boundary saturation and grain growth. *Scr. Mater.* (2004).

54. Krill, C. E., Ehrhardt, H. & Birringer, R. Thermodynamic stabilization of nanocrystallinity. *Zeitschrift fuer Met. Res. Adv. Tech.* (2005).

55. Kahlweit, M., Article, I. N. T., Microemulsions, O. N. S. & Gemny, W. Microemulsions. *Science (80-.).* **240**, 617–621 (1988).

56. Detor, A. J. & Schuh, C. A. Grain boundary segregation, chemical ordering and stability of nanocrystalline alloys: Atomistic computer simulations in the Ni-W system. *Acta Mater.* (2007).

57. O'Brien, C. J., Barr, C. M., Price, P. M., Hattar, K. & Foiles, S. M. Grain boundary phase transformations in PtAu and relevance to thermal stabilization of bulk nanocrystalline metals. *J. Mater. Sci.* **53**, 2911–2927 (2018).

58. Gibbs, J. W. The collected works of J. W. Gibbs: Thermodynamics. *London, Longmans, Green, co.* (1928).

59. Sutton, A. & Balluffi, R. *Interfaces in Crystalline Materials*. (2006).

60. Ishida, K. Effect of grain size on grain boundary segregation. *J. Alloys Compd.* **235**, 244–249 (1996).

61. Swaminarayan, S. & Srolovitz, D. J. Surface segregation in thin films. *Acta Mater.* **44**, 2067–2072 (1996).

62. Kirchheim, R. Grain coarsening inhibited by solute segregation. *Acta Mater.* **50**, 413–419 (2002).

63. Liu, F. & Kirchheim, R. Nano-scale grain growth inhibited by reducing grain boundary energy through solute segregation. *J. Cryst. Growth* **264**, 385–391 (2004).

64. Meng, Q. P., Rong, Y. H. & Hsu (Xu Zuyao), T. Y. Distribution of solute atoms in nanocrystalline materials. *Mater. Sci. Eng. A* **471**, 22–27 (2007).

65. Darling, K. A. *et al.* Stabilized nanocrystalline iron-based alloys: Guiding efforts in alloy selection. *Mater. Sci. Eng. A* **528**, 4365–4371 (2011).

66. Darling, K. A., Tschopp, M. A., VanLeeuwen, B. K., Atwater, M. & Liu, Z. K. Mitigating grain growth in binary nanocrystalline alloys through solute selection based on thermodynamic stability maps. *Comput. Mater. Sci.* **84**, 255–266 (2014).

67. Zhou, N. & Luo, J. Developing thermodynamic stability diagrams for equilibrium-grain-size binary alloys. *Mater. Lett.* **115**, 268–271 (2014).

68. Liang, T., Chen, Z., Yang, X., Zhang, J. & Zhang, P. The thermodynamic stability induced by solute co-segregation in nanocrystalline ternary alloys. *Int. J. Mater. Res.* **108**, 435–440 (2017).

69. Zhou, N., Hu, T., Huang, J. & Luo, J. Stabilization of nanocrystalline alloys at high temperatures via utilizing high-entropy grain boundary complexions. *Scr. Mater.* **124**, 160–163 (2016).

70. Gong, M. M. *et al.* Effects of concurrent grain boundary and surface segregation on the final stage of sintering: the case of Lanthanum doped yttria-stabilized zirconia. *J. Mater. Sci. Technol.* **33**, 251–260 (2017).

71. Trelewicz, J. R. & Schuh, C. A. Grain boundary segregation and thermodynamically stable binary nanocrystalline alloys. *Phys. Rev. B - Condens. Matter Mater. Phys.* **79**, 1–13 (2009).

72. Gong, M. M., Liu, F. & Zhang, K. Thermodynamic stability of binary nanocrystalline alloys: Analysis of solute and excess vacancy. *Appl. Phys. A Mater. Sci. Process.* **105**, 927–934 (2011).

73. Murdoch, H. A. & Schuh, C. A. Stability of binary nanocrystalline alloys against grain growth and phase separation. *Acta Mater.* **61**, 2121–2132 (2013).

74. Murdoch, H. A. & Schuh, C. A. Estimation of grain boundary segregation enthalpy and its role in stable nanocrystalline alloy design. *J. Mater. Res.* **28**, 2154–2163 (2013).

75. Saber, M., Kotan, H., Koch, C. C. & Scattergood, R. O. A predictive model for thermodynamic stability of grain size in nanocrystalline ternary alloys. *J. Appl. Phys.* **114**, (2013).

76. Saber, M., Kotan, H., Koch, C. C. & Scattergood, R. O. Thermodynamic stabilization of nanocrystalline binary alloys. *J. Appl. Phys.* **113**, (2013).

77. Chookajorn, T. & Schuh, C. A. Thermodynamics of stable nanocrystalline alloys: A monte carlo analysis. *Phys. Rev. B - Condens. Matter Mater. Phys.* **89**, 064102 (2014).

78. Kalidindi, A. R., Chookajorn, T. & Schuh, C. A. Nanocrystalline Materials at Equilibrium: A Thermodynamic Review. *Jom* **67**, 2834–2843 (2015).

79. Saber, M., Koch, C. C. & Scattergood, R. O. Thermodynamic grain size stabilization models: An overview. *Mater. Res. Lett.* **3**, 65–75 (2015).

80. Lupis, C. H. P. *Chemical thermodynamics of Materials*. (North Holland, 1983).

81. Clark, B. G. *et al.* Thermal Stability Comparison of Nanocrystalline Fe-Based Binary Alloy Pairs. *JOM* **68**, 1625–1633 (2016).

82. Chookajorn, T., Park, M. & Schuh, C. A. Duplex nanocrystalline alloys: Entropic nanostructure stabilization and a case study on W-Cr. *J. Mater. Res.* **30**, 151–163 (2014).

83. Amram, D. & Schuh, C. A. Higher Temperatures Yield Smaller Grains in a Thermally Stable Phase-Transforming Nanocrystalline Alloy. *Phys. Rev. Lett.* **121**, 145503–1 (2018).

84. Xing, W., Kalidindi, A. R. & Schuh, C. A. Preferred nanocrystalline configurations in ternary and multicomponent alloys. *Scr. Mater.* **127**, 136–140 (2017).

85. Ahadi, A. *et al.* The role of W on the thermal stability of nanocrystalline NiTiWx thin films. *Acta Mater.* **142**, 181–192 (2018).

86. Xing, W., Kalidindi, A. R., Amram, D. & Schuh, C. A. Solute interaction effects on grain boundary segregation in ternary alloys. *Acta Mater.* **161**, 285–294 (2018).

87. Xing, W. *et al.* Stability of ternary nanocrystalline alloys in the Pt-Pd-Au system. *Materialia* **8**, 100449 (2019).

88. Murdoch, H. A. & Schuh, C. A. Stability of binary nanocrystalline alloys against grain growth and phase separation. *Acta Mater.* **61**, 2121–2132 (2013).

89. Chookajorn, T. & Schuh, C. A. Nanoscale segregation behavior and high-temperature stability of nanocrystalline W-20 at.% Ti. *Acta Mater.* **73**, 128–138 (2014).

90. Chen, S. L., Kao, C. R. & Chang, Y. A. A generalized quasi-chemical model for ordered multi-component, multi-sublattice intermetallic compounds with anti-structure defects. *Intermetallics* **3**, 233–242 (1995).

91. Miedema, A. R., de Châtel, P. F. & de Boer, F. R. Cohesion in alloys - fundamentals of a semi-empirical model. *Phys. B* 1–28 (1980).

92. de Boer, F. R., Boom, R., Mattens, W. C. M., Miedema, A. R. & Niessen, A. K. *Cohesion in Metals: Transition Metal Alloys*. (North Holland, 1988).

93. Bakker, H. *Enthalpies in alloys, Miedema's semi-empirical model*. *Trans Tech Publications Ltd* (1998).

94. López, J. M. & Alonso, J. A. Semiempirical Theory of Solid Solubility in Transition Metal Alloys. *Zeitschrift fur Naturforsch.* **40a**, 1199–1205 (1985).

95. Zhao, S. Z., Li, J. H. & Liu, B. X. Thermodynamic prediction of metastable phases of Ni-Ti system formed by ion beam mixing. *Sci. China Technol. Sci.* **55**, 921–926 (2012).

96. http://www.crct.polymtl.ca/fact/phase_diagram.php?file=Ti-W.jpg&dir=SGTE2017.

97. *CALPHAD (Calculation of phase diagrams): A comprehensive guide*. (Pergamon, 1998).

98. Rohrer, G. S. Grain boundary energy anisotropy: A review. *J. Mater. Sci.* **46**, 5881–5895 (2011).

99. Zheng, H. *et al.* Grain Boundary Properties of Elemental Metals. *Preprint submitted*

to Acta Materialia (2019).

100. Wolf, D. Structure-energy correlation for grain boundaries in F.C.C. metals-III. Symmetrical tilt boundaries. *Acta Metall. Mater.* **38**, 781–790 (1990).

101. Homer, E. R., Hensley, D. M., Rosenbrock, C. W., Nguyen, A. H. & Hart, G. L. W. Machine-Learning Informed Representations for Grain Boundary Structures. *Front. Mater.* **6**, 168 (2019).

102. Swalin, R. A. *Thermodynamics of solids*. (John Wiley & Sons).

103. Miedema, A. R. SURFACE SEGREGATION IN ALLOYS OF TRANSITION METALS. *Zeitschrift fuer Met.* **69**, 455–461 (1978).

104. Tanaka, T., Hack, K., Iida, T. & Hara, S. Application of thermodynamic databases to the evaluation of surface tensions of molten alloys, salt mixtures and oxide mixtures. *Zeitschrift fuer Met. Res. Adv. Tech.* **87**, 380–389 (1996).

105. Kang, Y. B. Relationship between surface tension and Gibbs energy, and application of Constrained Gibbs Energy Minimization. *Calphad Comput. Coupling Phase Diagrams Thermochem.* **50**, 23–31 (2015).

106. Kaptay, G. Modelling equilibrium grain boundary segregation, grain boundary energy and grain boundary segregation transition by the extended Butler equation. *J. Mater. Sci.* **51**, 1738–1755 (2016).

107. Kaptay, G. Thermodynamic Stability of Nano-grained Alloys Against Grain Coarsening and Precipitation of Macroscopic Phases. *Metall. Mater. Trans. A* **50**, 4931–4947 (2019).

108. Suryanarayana, C. *Mechanical Alloying and Milling Mechanical Engineering*. *Progress in Materials Science* (2001).

109. Baláž, P. *et al.* Hallmarks of mechanochemistry: From nanoparticles to technology. *Chem. Soc. Rev.* **42**, 7571 (2013).

110. Suryanarayana, C. Recent developments in mechanical alloying. *Rev. Adv. Mater. Sci.* **18**, 203–211 (2008).

111. Koch, C. C. The Synthesis of Non-Equilibrium Structures by Ball-Milling. *Mater. Sci. Forum* **243**, 88–90 (1992).

112. Takacs, L. Solid state reactions induced by ball milling. *Hyperfine Interact.* **111**, 245–250 (1998).

113. Delogu, F. & Cocco, G. Kinetics of structural evolution in immiscible Ag-Cu and Co-Cu systems under mechanical processing conditions. *Mater. Sci. Eng. A* **402**, 208–214 (2005).

114. Mousavi, T. *et al.* A new approach to fabricate superconducting NbTi alloys. *Supercond. Sci. Technol.* **30**, 094001 (2017).

115. Baláž, P. *Mechanochemistry in nanoscience and minerals engineering*. *Mechanochemistry in Nanoscience and Minerals Engineering* (Springer, 2008).

116. Liu, K. W. & Mücklich, F. Thermal stability of nano-RuAl produced by ball milling. *Acta Mater.* **49**, 395–403 (2001).

117. http://www.crct.polymtl.ca/fact/phase_diagram.php?file=Al-W.jpg&dir=SGTE2017.

118. Orrù, R., Licheri, R., Locci, A. M., Cincotti, A. & Cao, G. Consolidation/synthesis of materials by electric current activated/assisted sintering. *Mater. Sci. Eng. R Reports* **12**, 127–287 (2009).

119. Waseda, Y., Matsubara, E. & Shinoda, K. *X-Ray Diffraction Crystallography*. *X-Ray Diffraction Crystallography* (Springer, 2011).

120. Rietveld, H. M. The Rietveld method. *Phys. Scr.* **89**, 098002 (2014).

121. Lutterotti, L. Maud: a Rietveld analysis program designed for the internet and experiment integration. *Acta Crystallogr. Sect. A Found. Crystallogr.* (2000).

122. Budrugeac, P. & Segal, E. Applicability of the Kissinger equation in thermal analysis. *J. Therm. Anal. Calorim.* **88**, 703–707 (2007).

123. da Costa, F. A., da Silva, A. G. P., Filho, F. A., Gomes, U. U. & Vieira, F. A. Synthesis of a nanocrystalline composite W-25 wt.%Ag powder by high energy milling. *Powder Technol.* **188**, 30–33 (2008).

124. Garroni, S., Enzo, S. & Delogu, F. Mesostructural refinement in the early stages of mechanical alloying. *Scr. Mater.* **83**, 49–52 (2014).

125. Da Pozzo, A., Palmas, S., Vacca, A. & Delogu, F. On the role of mechanical properties in the early stages of the mechanical alloying of Ag 50Cu 50 powder mixtures. *Scr. Mater.* **67**, 104–107 (2012).

126. Xu, J., Herr, U., Klassen, T. & Averback, R. S. Formation of supersaturated solid solutions in the immiscible Ni-Ag system by mechanical alloying. *J. Appl. Phys.* **79**, 3935 (1996).

127. Botcharova, E., Freudenberger, J. & Schultz, L. Mechanical alloying of copper with niobium and molybdenum. *J. Mater. Sci.* **39**, 5287–5290 (2004).

128. Wang, M. *et al.* Forced atomic mixing during severe plastic deformation: Chemical interactions and kinetically driven segregation. *Acta Mater.* **66**, 1–11 (2014).

129. Tang, H. G., Ma, X. F., Zhao, W., Yan, X. W. & Hong, R. J. Preparation of W–Al alloys by mechanical alloying. *J. Alloys Compd.* **347**, 228–230 (2002).

130. Zhang, H., Feng, P. & Akhtar, F. Aluminium matrix tungsten aluminide and tungsten reinforced composites by solid-state diffusion mechanism. *Sci. Rep.* **7**, 1–8 (2017).

List of publications

F.Torre, E. Musu, P. Barra, T. Huminiuc, T. Polcar, A. Locci, F. Delogu, Fabrication of W-Al nanocrystalline alloys by mechanical alloying. In progress.

F.Torre, T. Huminiuc, A. Locci, A. Rinaldi, F. Delogu, T. Polcar, C. A. Schuh, Thermodynamics-based design of coarsening-resistant nanocrystalline W alloys. In progress.

A. Locci, F. Torre, F. Delogu, Thermodynamic modelling of polycrystalline multicomponent multiphase metal alloys. Submitted to Modelling and Simulation in Materials Science and Engineering, and currently under revision.

B. N. Ezealigo, R. Orrù, F. Torre, P. C. Ricci, F. Delogu, G. Cao, Annealing effects on the structural and optical properties of undoped and Zr-doped Ba titanate prepared by self-propagating high-temperature synthesis. Submitted to ceramics international, and currently under revision.

F. Torre, V. Farina, A. Taras, C. Pistidda, A. Santoru, J. Bednarcik, G. Mulas, S. Enzo, S. Garroni, Room temperature hydrocarbon generation in olivine powders: Effect of mechanical processing under CO_2. Powder Technology, 2019. Article in press.

V. Farina, N. S. Gamba, F. Gennari, S. Garroni, F. Torre, A. Taras, S. Enzo, G. Mulas, CO_2 hydrogenation induced by machanochemical activation of olivine with water under CO_2 atmosphere. Frontiers in Energy Research, 7 (2019) 00107.

A. Valentoni, P. Barra, N. Senes, G. Mulas, C. Pistidda, J. Bednarcik, F. Torre, S. Garroni, S. Enzo. A mechanochemical route for the synthesis of $VNbO_5$ and its structural re-investigation using structure solution from powder diffraction data. Dalton Transactions, 48 (2019) 10986-10995.

F. Torre, G. Pia, M. Carta, L. Takacs, F. Delogu. Grain size reduction in Cu powders subjected to ball milling and ball drop experiments. Materials letters 232 (2018) 33-35.

B. Lasio, F. Torre, R. Orrù, G. Cao, M Cabibbo, F. Delogu, Fabrication of Cu-graphite metal matrix composites by ball milling and spark plasma sintering. Materials Letters 230 (2018) 199-202.

List of schools and conferences

Schools and seminars

Training school “Substitution of CRM: preparation of extreme materials by application of HP-HT and SPS methods”, 7-8 February 2019,The Institute of Advanced Manufacturing Technology, Krakow, Poland.

Training School “CRMs in extreme conditions: focus to young material scientist, challenges and perspectives”, 9 July 2018, FEMS Junior EUROMAT. Budapest, Hungary.

“ICARUS & SUPERMAT International Spring School on Forefront Alloys & Advanced Materials for Extreme Conditions”, 15-17 May 2017, Chia, Italy.

Training school "The challenge of CRMs in extreme condition: advanced multidisciplinary view".6-7 February 2017, Instituto Técnico Superior, Lisbon, Portugal.

Seminar “The history of mechanochemistry” by Prof. L. Takacs, 20 January 2017, Department of Chemistry Sassari, Italy.

Conferences

FEMS Junior EUROMAT 2018, July 8-12 2018, Budapest, Hungary, Poster presentation: Fabrication of graphite-reinforced Cu matrix composites.

SUPERMAT and ICARUS International Spring School 2017, 15-17 May 2017, Hotel Chia Laguna, Italy, Poster presentation: Generation of hydrocarbons by serpentinization of olivine in a simulated martian atmosphere.

E MRS Fall 2017 Warsaw Poland 18-20 September 2017, Poster presentation: Mechanical Processing of Cu-graphite powders mixtures and subsequent consolidation.

INCOME 2017 Kosice, Slovakia 4-6 September 2017, Poster presentation: Thermodynamically stable nanostructured metal alloys by mechanical alloying: The ICARUS project.

Appendix

Model details

The partition function Q of a substitutional solution can be defined as

$$Q = \Gamma exp\left(\frac{U}{k_B T}\right) \quad (1)$$

where U is the internal energy of the system and Γ the degeneracy factor. Once Q has been determined, the thermodynamic properties of the solution may be readily obtained.

The Helmholtz free energy is related to Q by the expression

$$F = k_B T\ lnQ \quad (2)$$

For solids and liquids at ordinary pressures, the Gibbs free energy may be assumed equivalent to the Helmholtz free energy, being the term pV usually negligible. This makes any assumption regarding the volume of atomic species and of the overall system (i.e. excess volume effect) unnecessary. It follows that

$$G \approx -k_B T\ lnQ \quad (3)$$

The combination of Eqs. 1 and 3 results in the expression

$$G = -k_B T\ ln\Gamma + U \quad (4)$$

Let us consider a system consisting of n components and a total number of atoms equal to N. Since there are $N!$ different ways of distributing N atoms among N lattice sites, the degeneracy factor can be expressed as

$$\Gamma = \frac{N!}{\prod_{i=1}^{n} N_i!} \tag{5}$$

where N_i is the number of atoms of the *i*-th component. Substituting Eq. 5 into Eq. 4, we obtain

$$G = -k_B T \left(lnN! - ln \prod_{i=1}^{n} N_i!\right) + U \tag{6}$$

Using Stirling's approximation,

$$ln\Gamma \approx (lnN - 1) - \sum_{i=1}^{n} N_i (lnN_i - 1) \tag{7}$$

being

$$N = \sum_{i=1}^{n} N_i \tag{8}$$

$$ln\Gamma \approx NlnN - \sum_{i=1}^{n} N_i lnN_i \tag{9}$$

$$ln\Gamma \approx \sum_{i=1}^{n} N_i lnN - \sum_{i=1}^{n} N_i lnN_i \tag{10}$$

$$ln\Gamma \approx \sum_{i=1}^{n} N_i (lnN - lnN_i) \tag{11}$$

$$ln\Gamma \approx \sum_{i=1}^{n} N_i ln\left(\frac{N}{N_i}\right) \tag{12}$$

$$ln\Gamma \approx -\sum_{i=1}^{n} N_i lnx_i \tag{13}$$

Then, Eq. 6 can be written as

$$G = k_B T \sum_{i=1}^{n} N_i ln x_i + U \quad (14)$$

If the internal energy of mixing is defined as

$$\Delta U_{mix} = U - U^0 \quad (15)$$

we have that

$$G = k_B T \sum_{i=1}^{n} N_i ln x_i + U^0 + \Delta U_{mix} \quad (16)$$

Under the assumption that $pV \approx 0$, the Gibbs free energy can be also expressed as

$$G = U - TS \quad (17)$$

A simple rearrangement leads to

$$G = U^0 + \Delta U_{mix} - T(S^0 + \Delta S_{mix}) \quad (18)$$

$$G = U^0 - TS^0 + \Delta U_{mix} - T\Delta S_{mix} \quad (19)$$

$$G = G^0 + \Delta G_{mix} \quad (20)$$

At 0 *K*, the entropy of the system in its reference state is zero. Then, Eqs. 16 and 20 can be combined to give

$$\Delta G_{mix} = k_B T \sum_{i=1}^{n} N_i ln x_i + \Delta U_{mix} \quad (21)$$

For sake of generality, we can also assume that the system consists of π phases. Accordingly, Eq. 21 can be rewritten as

$$\Delta G_{mix}^{(k)} = k_B T \sum_{i=1}^{n} N_i^{(k)} ln x_i^{(k)} + \Delta U_{mix}^{(k)} \; ; \;\; k = 1, .., \pi \tag{22}$$

Taking advantage of the regular solution model, the internal energy of the *k*-th phase can be expressed as

$$U^{(k)} = \sum_{i=1}^{n} \sum_{j=i}^{n} \widetilde{N}_{ij}^{(k)} u_{ij}^{(k)} \;\; k = 1, .., \pi \tag{23}$$

where $\widetilde{N}_{ij}^{(k)}$ and $u_{ij}^{(k)}$ represent, respectively, the number of *i-j* pairs (bonds) and their energy in the *k*-th phase. Alternatively, Eq. 23 can be written as

$$U^{(k)} = \sum_{i=1}^{n} \widetilde{N}_{ii}^{(k)} u_{ii}^{(k)} + \sum_{i=1}^{n} \sum_{j=i+1}^{n} \widetilde{N}_{ij}^{(k)} u_{ij}^{(k)} \;\; k = 1, .., \pi \tag{24}$$

Therefore, the system internal energy will result from summing up the internal energies of all the phases composing the system at equilibrium. It follows that

$$U = \sum_{k=1}^{q} \left(\sum_{i=1}^{n} \widetilde{N}_{ii}^{(g_k)} u_{ii}^{(g_k)} + \sum_{i=1}^{n} \sum_{j=i+1}^{n} \widetilde{N}_{ij}^{(g_k)} u_{ij}^{(g_k)} \right) + \sum_{i=1}^{n} \widetilde{N}_{ii}^{(ig)} u_{ii}^{(ig)} + \sum_{i=1}^{n} \sum_{j=i+1}^{n} \widetilde{N}_{ij}^{(ig)} u_{ij}^{(ig)} \tag{25}$$

On the other hand, the internal energy of the system in its reference state (i.e. before mixing) is given by

$$U^0 = \sum_{i=1}^{n} \frac{Z_i^0}{2} N_i \, u_{ii}^0 \tag{26}$$

where Z_i^0 and u_{ii}^0 are, respectively, the coordination number and the bond energy of the *i*-th component in its reference state.

Since the system is closed, the following material balance holds:

$$N_i = \sum_{k=1}^{q} N_i^{(g_k)} + N_i^{(ig)}; i = 1,..,n \tag{27}$$

In the presence of A, B, C, … atomic species, any given atom A forms Z pairs of the various AA, AB, AC, … types. The number of A atoms and the number of pairs in which A atoms are involved are related to each other. Then, if the summation is extended to all types of atoms in the different system regions, one obtains that

$$\frac{Z^{(l)}}{2} N_i^{(l)} = \widetilde{N}_{ii}^{(l)} + \frac{1}{2}\sum_{j\neq i=1}^{n} \widetilde{N}_{ij}^{(l)}; i = 1,..,n;\ l = g_k, ig; k = 1,..,q \tag{28}$$

or, alternatively

$$N_i^{(l)} = \frac{2}{Z^{(l)}}\left(\widetilde{N}_{ii}^{(l)} + \frac{1}{2}\sum_{j\neq i=1}^{n} \widetilde{N}_{ij}^{(l)}\right); i = 1,..,n;\ l = g_k, ig; k = 1,..,q \tag{29}$$

which shows how the coordination number can be different for each phase.

Substituting Eq. 27 into Eq. 26, the internal energy of the system in its reference state can be expressed as

$$U^0 = \sum_{i=1}^{n} \frac{Z_i^0}{2}\left(\sum_{k=1}^{q} N_i^{(g_k)} + N_i^{(ig)}\right) u_{ii}^0 \tag{30}$$

and taking advantage of Eq. 29

$$U^0 = \sum_{i=1}^{n} \frac{Z_i^0}{2}\left[\begin{array}{c}\sum_{k=1}^{q} \frac{2}{Z^{(g_k)}}\left(\widetilde{N}_{ii}^{(g_k)} + \frac{1}{2}\sum_{j\neq i=1}^{n} \widetilde{N}_{ij}^{(g_k)}\right) + \\ \frac{2}{Z^{(ig)}}\left(\widetilde{N}_{ii}^{(ig)} + \frac{1}{2}\sum_{j\neq i=1}^{n} \widetilde{N}_{ij}^{(ig)}\right)\end{array}\right] u_{ii}^0 \tag{31}$$

Rearranging,

$$U^0 = \sum_{i=1}^{n}\left[\sum_{k=1}^{q} \frac{Z_i^0}{Z^{(g_k)}}\left(\widetilde{N}_{ii}^{(g_k)} + \frac{1}{2}\sum_{j\neq i=1}^{n} \widetilde{N}_{ij}^{(g_k)}\right) + \frac{Z_i^0}{Z^{(ig)}}\left(\widetilde{N}_{ii}^{(ig)} + \frac{1}{2}\sum_{j\neq i=1}^{n} \widetilde{N}_{ij}^{(ig)}\right)\right] u_{ii}^0 \tag{32}$$

$$U^0 = \sum_{i=1}^{n} \left[\begin{matrix} \sum_{k=1}^{q} \frac{Z_i^0}{Z^{(g_k)}} \widetilde{N}_{ii}^{(g_k)} + \frac{1}{2} \sum_{k=1}^{q} \sum_{j \neq i=1}^{n} \frac{Z_i^0}{Z^{(g_k)}} \widetilde{N}_{ij}^{(g_k)} + \\ \frac{Z_i^0}{Z^{(ig)}} \widetilde{N}_{ii}^{(ig)} + \frac{1}{2} \sum_{j \neq i=1}^{n} \frac{Z_i^0}{Z^{(ig)}} \widetilde{N}_{ij}^{(ig)} \end{matrix} \right] u_{ii}^0 \tag{33}$$

$$U^0 = \sum_{i=1}^{n} \left[\begin{matrix} \sum_{k=1}^{q} \frac{Z_i^0}{Z^{(g_k)}} \widetilde{N}_{ii}^{(g_k)} + \frac{Z_i^0}{Z^{(ig)}} \widetilde{N}_{ii}^{(ig)} + \\ + \frac{1}{2} \left(\sum_{k=1}^{q} \sum_{j \neq i=1}^{n} \frac{Z_i^0}{Z^{(g_k)}} \widetilde{N}_{ij}^{(g_k)} + \sum_{j \neq i=1}^{n} \frac{Z_i^0}{Z^{(ig)}} \widetilde{N}_{ij}^{(ig)} \right) \end{matrix} \right] u_{ii}^0 \tag{34}$$

$$U^0 = \sum_{i=1}^{n} \left[\begin{matrix} \sum_{k=1}^{q} \frac{Z_i^0}{Z^{(g_k)}} \widetilde{N}_{ii}^{(g_k)} u_{ii}^0 + \frac{Z_i^0}{Z^{(ig)}} \widetilde{N}_{ii}^{(ig)} u_{ii}^0 + \\ \frac{1}{2} \left(\sum_{k=1}^{q} \sum_{j \neq i=1}^{n} \frac{Z_i^0}{Z^{(g_k)}} \widetilde{N}_{ij}^{(g_k)} u_{ii}^0 + \sum_{j \neq i=1}^{n} \frac{Z_i^0}{Z^{(ig)}} \widetilde{N}_{ij}^{(ig)} u_{ii}^0 \right) \end{matrix} \right] \tag{35}$$

$$U^0 = \sum_{i=1}^{n} \sum_{k=1}^{q} \frac{Z_i^0}{Z^{(g_k)}} \widetilde{N}_{ii}^{(g_k)} u_{ii}^0 + \sum_{i=1}^{n} \frac{Z_i^0}{Z^{(ig)}} \widetilde{N}_{ii}^{(ig)} u_{ii}^0 + \frac{1}{2} \sum_{i=1}^{n} \sum_{k=1}^{q} \sum_{j \neq i=1}^{n} \frac{Z_i^0}{Z^{(g_k)}} \widetilde{N}_{ij}^{(g_k)} u_{ii}^0 + \frac{1}{2} \sum_{i=1}^{n} \sum_{j \neq i=1}^{n} \frac{Z_i^0}{Z^{(ig)}} \widetilde{N}_{ij}^{(ig)} u_{ii}^0 \tag{36}$$

$$U^0 = \sum_{k=1}^{q} \sum_{i=1}^{n} \frac{Z_i^0}{Z^{(g_k)}} \widetilde{N}_{ii}^{(g_k)} u_{ii}^0 + \sum_{i=1}^{n} \frac{Z_i^0}{Z^{(ig)}} \widetilde{N}_{ii}^{(ig)} u_{ii}^0 + \frac{1}{2} \sum_{k=1}^{q} \sum_{i=1}^{n} \sum_{j \neq i=1}^{n} \frac{Z_i^0}{Z^{(g_k)}} \widetilde{N}_{ij}^{(g_k)} u_{ii}^0 + \frac{1}{2} \sum_{i=1}^{n} \sum_{j \neq i=1}^{n} \frac{Z_i^0}{Z^{(ig)}} \widetilde{N}_{ij}^{(ig)} u_{ii}^0 \tag{37}$$

$$U^0 = \sum_{k=1}^{q} \sum_{i=1}^{n} \frac{Z_i^0}{Z^{(g_k)}} \widetilde{N}_{ii}^{(g_k)} u_{ii}^0 + \sum_{i=1}^{n} \frac{Z_i^0}{Z^{(ig)}} \widetilde{N}_{ii}^{(ig)} u_{ii}^0 + \frac{1}{2} \sum_{k=1}^{q} \sum_{i=1}^{n} \left(\sum_{j=1}^{i-1} \frac{Z_i^0}{Z^{(g_k)}} \widetilde{N}_{ij}^{(g_k)} u_{ii}^0 + \sum_{j=i+1}^{n} \frac{Z_i^0}{Z^{(g_k)}} \widetilde{N}_{ij}^{(g_k)} u_{ii}^0 \right) + \frac{1}{2} \sum_{i=1}^{n} \left(\sum_{j=1}^{i-1} \frac{Z_i^0}{Z^{(ig)}} \widetilde{N}_{ij}^{(ig)} u_{ii}^0 + \sum_{j=i+1}^{n} \frac{Z_i^0}{Z^{(ig)}} \widetilde{N}_{ij}^{(ig)} u_{ii}^0 \right) \tag{38}$$

$$U^0 = \sum_{k=1}^{q} \sum_{i=1}^{n} \frac{Z_i^0}{Z^{(g_k)}} \widetilde{N}_{ii}^{(g_k)} u_{ii}^0 + \sum_{i=1}^{n} \frac{Z_i^0}{Z^{(ig)}} \widetilde{N}_{ii}^{(ig)} u_{ii}^0 + \frac{1}{2} \sum_{k=1}^{q} \sum_{i=1}^{n} \left(\sum_{j=i+1}^{n} \frac{Z_j^0}{Z^{(g_k)}} \widetilde{N}_{ji}^{(g_k)} u_{jj}^0 + \sum_{j=i+1}^{n} \frac{Z_i^0}{Z^{(g_k)}} \widetilde{N}_{ij}^{(g_k)} u_{ii}^0 \right) + \frac{1}{2} \sum_{i=1}^{n} \left(\sum_{j=i+1}^{n} \frac{Z_j^0}{Z^{(ig)}} \widetilde{N}_{ji}^{(ig)} u_{jj}^0 + \sum_{j=i+1}^{n} \frac{Z_i^0}{Z^{(ig)}} \widetilde{N}_{ij}^{(ig)} u_{ii}^0 \right) \tag{39}$$

being $\widetilde{N}_{ij} = \widetilde{N}_{ji}$,

$$U^0 = \sum_{k=1}^{q}\sum_{i=1}^{n}\frac{Z_i^0}{Z^{(g_k)}}\widetilde{N}_{ii}^{(g_k)}u_{ii}^0 + \sum_{i=1}^{n}\frac{Z_i^0}{Z^{(ig)}}\widetilde{N}_{ii}^{(ig)}u_{ii}^0 + \frac{1}{2}\sum_{k=1}^{q}\sum_{i=1}^{n}\left(\sum_{j=i+1}^{n}\frac{Z_j^0}{Z^{(g_k)}}\widetilde{N}_{ij}^{(g_k)}u_{jj}^0 + \sum_{j=i+1}^{n}\frac{Z_i^0}{Z^{(g_k)}}\widetilde{N}_{ij}^{(g_k)}u_{ii}^0\right) + \frac{1}{2}\sum_{i=1}^{n}\left(\sum_{j=i+1}^{n}\frac{Z_j^0}{Z^{(ig)}}\widetilde{N}_{ij}^{(ig)}u_{jj}^0 + \sum_{j=i+1}^{n}\frac{Z_i^0}{Z^{(ig)}}\widetilde{N}_{ij}^{(ig)}u_{ii}^0\right) \quad (40)$$

$$U^0 = \sum_{k=1}^{q}\sum_{i=1}^{n}\frac{Z_i^0}{Z^{(g_k)}}\widetilde{N}_{ii}^{(g_k)}u_{ii}^0 + \sum_{i=1}^{n}\frac{Z_i^0}{Z^{(ig)}}\widetilde{N}_{ii}^{(ig)}u_{ii}^0 + \frac{1}{2}\sum_{k=1}^{q}\sum_{i=1}^{n}\sum_{j=i+1}^{n}\widetilde{N}_{ij}^{(g_k)}\left(\frac{Z_i^0}{Z^{(g_k)}}u_{ii}^0 + \frac{Z_j^0}{Z^{(g_k)}}u_{jj}^0\right) + \frac{1}{2}\sum_{i=1}^{n}\sum_{j=i+1}^{n}\widetilde{N}_{ij}^{(ig)}\left(\frac{Z_i^0}{Z^{(g_k)}}u_{ii}^0 + \frac{Z_j^0}{Z^{(g_k)}}u_{jj}^0\right) \quad (41)$$

When Eq. 41 is subtracted from Eq. 25, the following relationships are obtained:

$$\Delta U_{mix} = \sum_{k=1}^{q}\sum_{i=1}^{n}\widetilde{N}_{ii}^{(g_k)}u_{ii}^{(g)} + \sum_{k=1}^{q}\sum_{i=1}^{n}\sum_{j=i+1}^{n}\widetilde{N}_{ij}^{(g_k)}u_{ij}^{(g)} + \sum_{i=1}^{n}\widetilde{N}_{ii}^{(ig)}u_{ii}^{(ig)} + \sum_{i=1}^{n}\sum_{j=i+1}^{n}\widetilde{N}_{ij}^{(ig)}u_{ij}^{(ig)} - \sum_{k=1}^{q}\sum_{i=1}^{n}\frac{Z_i^0}{Z^{(g_k)}}\widetilde{N}_{ii}^{(g_k)}u_{ii}^0 - \sum_{i=1}^{n}\frac{Z_i^0}{Z^{(ig)}}\widetilde{N}_{ii}^{(ig)}u_{ii}^0 - \frac{1}{2}\sum_{k=1}^{q}\sum_{i=1}^{n}\sum_{j=i+1}^{n}\widetilde{N}_{ij}^{(g_k)}\left(\frac{Z_i^0}{Z^{(g_k)}}u_{ii}^0 + \frac{Z_j^0}{Z^{(g_k)}}u_{jj}^0\right) - \frac{1}{2}\sum_{i=1}^{n}\sum_{j=i+1}^{n}\widetilde{N}_{ij}^{(ig)}\left(\frac{Z_i^0}{Z^{(g_k)}}u_{ii}^0 + \frac{Z_j^0}{Z^{(g_k)}}u_{jj}^0\right) \quad (42)$$

$$\Delta U_{mix} = \sum_{k=1}^{q}\sum_{i=1}^{n}\left(u_{ii}^{(g)} - \frac{Z_i^0}{Z^{(g_k)}}u_{ii}^0\right)\widetilde{N}_{ii}^{(g_k)} + \sum_{k=1}^{q}\sum_{i=1}^{n}\sum_{j=i+1}^{n}\widetilde{N}_{ij}^{(g_k)}\left[u_{ij}^{(g)} - \frac{1}{2}\left(\frac{Z_i^0}{Z^{(g_k)}}u_{ii}^0 + \frac{Z_j^0}{Z^{(g_k)}}u_{jj}^0\right)\right] + \sum_{i=1}^{n}\widetilde{N}_{ii}^{(ig)}\left(u_{ii}^{(ig)} - \frac{Z_i^0}{Z^{(ig)}}u_{ii}^0\right) + \sum_{i=1}^{n}\sum_{j=i+1}^{n}\widetilde{N}_{ij}^{(ig)}\left[u_{ij}^{(ig)} - \frac{1}{2}\left(\frac{Z_i^0}{Z^{(g_k)}}u_{ii}^0 + \frac{Z_j^0}{Z^{(g_k)}}u_{jj}^0\right)\right] \quad (43)$$

Now, we can define the following parameters:

$$\omega_{ij}^{(l)} = u_{ij}^{(l)} - \frac{1}{2}\left(u_{ii}^{(l)} + u_{jj}^{(l)}\right); i,j = 1,..,n;\ l = g_k, ig; k = 1,..,q \quad (44)$$

$$\Delta u_{ii}^{(l)} = u_{ii}^{(l)} - \frac{Z_i^0}{Z^{(l)}}u_{ii}^0; i = 1,..,n;\ l = g_k, ig; k = 1,..,q \quad (45)$$

Combining Eqs. 44 and 45 yields

$$u_{ij}^{(l)} - \frac{1}{2}\frac{Z_i^0}{Z^{(l)}}\left(u_{jj}^0 + u_{ii}^0\right) = \omega_{ij}^{(l)} + \frac{1}{2}\left(\Delta u_{jj}^{(l)} + \Delta u_{ii}^{(l)}\right)\ i = 1,..,n;\ l = g_k, ig; k = 1,..,q \quad (46)$$

and, finally,

$$\Delta U_{mix} = \sum_{k=1}^{q}\sum_{i=1}^{n}\widetilde{N}_{ii}^{(g_k)}\Delta u_{ii}^{(g_k)} + \sum_{k=1}^{q}\sum_{i=1}^{n}\sum_{j=i+1}^{n}\widetilde{N}_{ij}^{(g_k)}\left[\omega_{ij}^{(g_k)} + \frac{1}{2}\left(\Delta u_{ii}^{(g_k)} + \Delta u_{jj}^{(g_k)}\right)\right] + \sum_{i=1}^{n}\widetilde{N}_{ii}^{(ig)}\Delta u_{ii}^{(ig)} + \sum_{i=1}^{n}\sum_{j=i+1}^{n}\widetilde{N}_{ij}^{(ig)}\left[\omega_{ij}^{(ig)} + \frac{1}{2}\left(\Delta u_{ii}^{(ig)} + \Delta u_{jj}^{(ig)}\right)\right] \quad (47)$$

The number of bonds of *i-j* pairs in grains and intergranular regions are related to the number of atoms of types *i* and *j* involved in each zone through the relationships:

$$\widetilde{N}_{ij}^{(l)} = \begin{cases} x_i^{(l)}x_j^{(l)}\widetilde{N}^{(l)}\ if\ i = j \\ 2x_i^{(l)}x_j^{(l)}\widetilde{N}^{(l)}\ if\ i \neq j \end{cases} i,j = 1,..,n;\ l = g_k, ig; k = 1,..,q \quad (48)$$

where $\widetilde{N}^{(l)}$ represents the total number of bonds in the phase *l*, and the atomic fractions are defined as

$$x_i^{(l)} = \frac{N_i^{(l)}}{N^{(l)}}; i = 1,..,n; l = g_k, ig; k = 1,..,q \quad (49)$$

The total number of bonds in each phase can be related to the total number of atoms in the same phase by the following relation:

$$\widetilde{N}^{(l)} = \frac{Z^{(l)}}{2}N^{(l)};\ l = g_k, ig; k = 1,..,q \quad (50)$$

Defining the atomic fraction of the region *l* as follows:

$$\theta^{(l)} = \frac{N^{(l)}}{N};\ l = g_k, ig;\ k = 1,..,q \tag{51}$$

Eq. 48 can be rewritten as

$$\widetilde{N}_{ij}^{(l)} = \begin{cases} \frac{Z^{(l)}}{2} x_i^{(l)} x_j^{(l)} \theta^{(l)} N \ if\ i = j \\ Z^{(l)} x_i^{(l)} x_j^{(l)} \theta^{(l)} N \ if\ i \neq j \end{cases} i,j = 1,..,n;\ l = g_k, ig; k = 1,..,q \tag{52}$$

Substituting Eq. 52 into Eq. 47 it can be obtained that

$$\begin{aligned} \Delta U_{mix} &= \sum_{k=1}^{q} \sum_{i=1}^{n} \frac{Z^{(g_k)}}{2} x_i^{(g_k)} x_i^{(g_k)} \theta^{(g_k)} N\, \Delta u_{ii}^{(g_k)} + \\ &\sum_{k=1}^{q} \sum_{i=1}^{n} \sum_{j=i+1}^{n} Z^{(g_k)} x_i^{(g_k)} x_j^{(g_k)} \theta^{(g_k)} N \left[\omega_{ij}^{(g_k)} + \frac{1}{2} \left(\Delta u_{ii}^{(g_k)} + \Delta u_{jj}^{(g_k)} \right) \right] + \\ &\sum_{i=1}^{n} \frac{Z^{(ig)}}{2} x_i^{(ig)} x_i^{(ig)} \theta^{(ig)} N \Delta u_{ii}^{(ig)} + \sum_{i=1}^{n} \sum_{j=i+1}^{n} Z^{(ig)} x_i^{(ig)} x_j^{(ig)} \theta^{(ig)} N \left[\omega_{ij}^{(ig)} + \frac{1}{2} \left(\Delta u_{ii}^{(ig)} + \Delta u_{jj}^{(ig)} \right) \right] \end{aligned} \tag{53}$$

Multiplying by the ratio N_{Av}/N, the molar internal energy of mixing is expressed as

$$\begin{aligned} \Delta \hat{u}_{mix} &= \sum_{k=1}^{q} \sum_{i=1}^{n} \frac{Z^{(g_k)}}{2} x_i^{(g_k)} x_i^{(g_k)} \theta^{(g_k)}\, \Delta u_{ii}^{(g_k)} + \\ &\sum_{k=1}^{q} \sum_{i=1}^{n} \sum_{j=i+1}^{n} Z^{(g_k)} x_i^{(g_k)} x_j^{(g_k)} \theta^{(g_k)} \left[\omega_{ij}^{(g_k)} + \frac{1}{2} \left(\Delta u_{ii}^{(g_k)} + \Delta u_{jj}^{(g_k)} \right) \right] + \\ &\sum_{i=1}^{n} \frac{Z^{(ig)}}{2} x_i^{(ig)} x_i^{(ig)} \theta^{(ig)} \Delta u_{ii}^{(ig)} + \sum_{i=1}^{n} \sum_{j=i+1}^{n} Z^{(ig)} x_i^{(ig)} x_j^{(ig)} \theta^{(ig)} \left[\omega_{ij}^{(ig)} + \frac{1}{2} \left(\Delta u_{ii}^{(ig)} + \Delta u_{jj}^{(ig)} \right) \right] \end{aligned} \tag{54}$$

Let us rearrange Eq. 54 as follows

$$\begin{aligned} \Delta \hat{u}_{mix} &= \sum_{k=1}^{q} \theta^{(g_k)} \sum_{i=1}^{n} \frac{Z^{(g_k)}}{2} x_i^{(g_k)} x_i^{(g_k)}\, \Delta u_{ii}^{(g_k)} + \\ &\sum_{k=1}^{q} \theta^{(g_k)} \sum_{i=1}^{n} \sum_{j=i+1}^{n} Z^{(g_k)} x_i^{(g_k)} x_j^{(g_k)} \left[\omega_{ij}^{(g_k)} + \frac{1}{2} \left(\Delta u_{ii}^{(g_k)} + \Delta u_{jj}^{(g_k)} \right) \right] + \end{aligned}$$

$$\theta^{(ig)}\sum_{i=1}^{n}\frac{Z^{(ig)}}{2}x_i^{(ig)}x_i^{(ig)}\Delta u_{ii}^{(ig)}+\theta^{(ig)}\sum_{i=1}^{n}\sum_{j=i+1}^{n}Z^{(ig)}x_i^{(ig)}x_j^{(ig)}\left[\omega_{ij}^{(ig)}+\frac{1}{2}\left(\Delta u_{ii}^{(ig)}+\Delta u_{jj}^{(ig)}\right)\right] \tag{55}$$

$$\Delta\hat{u}_{mix}=\sum_{k=1}^{q}\theta^{(g_k)}\left(\sum_{i=1}^{n}\frac{Z^{(g_k)}}{2}x_i^{(g_k)}x_i^{(g_k)}\,\Delta u_{ii}^{(g_k)}+\sum_{i=1}^{n}\sum_{j=i+1}^{n}Z^{(g_k)}x_i^{(g_k)}x_j^{(g_k)}\left[\omega_{ij}^{(g_k)}+\frac{1}{2}\left(\Delta u_{ii}^{(g_k)}+\Delta u_{jj}^{(g_k)}\right)\right]\right)+\theta^{(ig)}\left(\sum_{i=1}^{n}\frac{Z^{(ig)}}{2}x_i^{(ig)}x_i^{(ig)}\Delta u_{ii}^{(ig)}+\sum_{i=1}^{n}\sum_{j=i+1}^{n}Z^{(ig)}x_i^{(ig)}x_j^{(ig)}\left[\omega_{ij}^{(ig)}+\frac{1}{2}\left(\Delta u_{ii}^{(ig)}+\Delta u_{jj}^{(ig)}\right)\right]\right) \tag{56}$$

$$\Delta\hat{u}_{mix}=\sum_{k=1}^{q}\theta^{(g_k)}\Delta\hat{u}_{mix}^{(g_k)}+\theta^{(ig)}\Delta\hat{u}_{mix}^{(ig)} \tag{57}$$

where

$$\Delta\hat{u}_{mix}^{(g_k)}=\frac{Z^{(g_k)}}{2}\left\{\sum_{i=1}^{n}x_i^{(g_k)}x_i^{(g_k)}\,\Delta u_{ii}^{(g_k)}+\sum_{i=1}^{n}\sum_{j=i+1}^{n}2x_i^{(g_k)}x_j^{(g_k)}\left[\omega_{ij}^{(g_k)}+\frac{1}{2}\left(\Delta u_{ii}^{(g_k)}+\Delta u_{jj}^{(g_k)}\right)\right]\right\} \tag{58}$$

$$\Delta\hat{u}_{mix}^{(ig)}=\frac{Z^{(ig)}}{2}\sum_{i=1}^{n}x_i^{(ig)}x_i^{(ig)}\Delta u_{ii}^{(ig)}+\sum_{i=1}^{n}\sum_{j=i+1}^{n}2x_i^{(ig)}x_j^{(ig)}\left[\omega_{ij}^{(ig)}+\frac{1}{2}\left(\Delta u_{ii}^{(ig)}+\Delta u_{jj}^{(ig)}\right)\right] \tag{59}$$

Recalling Eq. 22, the Gibbs free energy of mixing is equal to

$$\Delta G_{mix}=k_BT\left(\sum_{k=1}^{q}\sum_{i=1}^{n}N_i^{(g_k)}lnx_i^{(g_k)}+\sum_{i=1}^{n}N_i^{(ig)}lnx_i^{(ig)}\right)+\Delta U_{mix} \tag{60}$$

Rearranging,

$$\Delta G_{mix}=k_BT\left(\sum_{k=1}^{q}N^{(g_k)}\sum_{i=1}^{n}x_i^{(g_k)}lnx_i^{(g_k)}+N^{(ig)}\sum_{i=1}^{n}x_i^{(ig)}lnx_i^{(ig)}\right)+\Delta U_{mix} \tag{61}$$

$$\Delta G_{mix} = Nk_BT\left(\sum_{k=1}^{q}\theta^{(g_k)}\sum_{i=1}^{n}x_i^{(g_k)}lnx_i^{(g_k)} + \theta^{(ig)}\sum_{i=1}^{n}x_i^{(ig)}lnx_i^{(ig)}\right) + \Delta U_{mix} \quad (62)$$

and multiplying by the ratio N_{Av}/N,

$$\Delta \hat{g}_{mix} = RT\left(\sum_{k=1}^{q}\theta^{(g_k)}\sum_{i=1}^{n}x_i^{(g_k)}lnx_i^{(g_k)} + \theta^{(ig)}\sum_{i=1}^{n}x_i^{(ig)}lnx_i^{(ig)}\right) + \Delta \hat{u}_{mix} \quad (63)$$

Eventually, the following material balances for the case of closed systems complete the mathematical model:

$$x_i^0 = \sum_{k=1}^{q}x_i^{(g_k)}\theta^{(g_k)} + x_i^{(ig)}\theta^{(ig)};\ i = 1,..n \quad (64)$$

where x_i^0 represents the global molar fraction of the *i*-th component.

It can be seen that the Gibbs free energy of mixing depends on bond energies, composition and the molar (atomic) fraction of the phases composing the system. In addition, phase molar fractions are related to the volumetric fractions through the following relation:

$$f^{(l)} = \frac{\theta^{(l)}\sum_{i=1}^{n}\Omega_i x_i^{(l)}}{\sum_{k=1}^{q}\left(\theta^{(g_k)}\sum_{i=1}^{n}\Omega_i x_i^{(g_k)}\right)+\theta^{(ig)}\sum_{i=1}^{n}\Omega_i x_i^{(ig)}};\ l = g_k, ig; k = 1,..,q \quad (66)$$

Nomenclature

d grain size (diameter);

f volumetric fraction;

F Helmholtz free energy;

G Gibbs free energy;

$\hat{g}$ molar Gibbs free energy;

$\hat{h}$ molar enthalpy;

k_B Boltzmann constant;

N number of atoms;

N_{Av} Avogadro number;

$\widetilde{N}$ number of bonds;

n number of components;

p pressure;

Q partition function;

q number of grained phases;

R universal gas constant;

S entropy;

t intergranular region thickness;

T temperature;

V volume;

U internal energy;

u bond energy;

$\hat{u}$ molar internal energy;

x atomic (molar) fraction of components;

Z coordination number;

Greek letters

Δ difference;

φ degree of freedom;

δ phase dimensionality;

Γ degeneracy factor;

θ atomic (molar) fraction of phases;

π number of phases;

ω atoms interaction energy;

Ω atomic volume;

Superscripts

$^{(b)}$ bulk;

$^{(g)}$ grained;

$^{(ig)}$ intergranular;

$^{(k)}$ k-th phase;

$^{(l)}$ l-th phase;

^{0} reference state;

* dimensionless;

$^{\infty}$ dilute solution;

Subscripts

$_{i}$ i-th component;

$_{j}$ j-th component;

$_{mix}$ mixing;

$_{seg}$ segregation.